Monthly Notices
of the
ROYAL ASTRONOMICAL SOCIETY

MNRAS **462,** 395–413 (2016)
Advance Access publication 2016 July 13

doi:10.1093/mnras/stw1685

Studying the evolution of AGB stars in the *Gaia* epoch

M. Di Criscienzo,[1⋆] P. Ventura,[1] D. A. García-Hernández,[2,3] F. Dell'Agli,[1] M. Castellani,[1] P. M. Marrese,[1,4] S. Marinoni,[1,4] G. Giuffrida[1,4] and O. Zamora[2,3]

[1]*INAF – Osservatorio Astronomico di Roma, Via Frascati 33, I-00040 Monte Porzio Catone (RM), Italy*
[2]*Instituto de Astrofísica de Canarias, E-38205 La Laguna, Tenerife, Spain*
[3]*Departamento de Astrofísica, Universidad de La Laguna (ULL), E-38206 La Laguna, Tenerife, Spain*
[4]*ASDC-ASI, Via del Politecnico, I-00133 Roma, Italy*

Accepted 2016 July 11. Received 2016 July 11; in original form 2016 May 19

ABSTRACT

We present asymptotic giant branch (AGB) models of solar metallicity, to allow the interpretation of observations of Galactic AGB stars, whose distances should be soon available after the first release of the *Gaia* catalogue. We find an abrupt change in the AGB physical and chemical properties, occurring at the threshold mass to ignite hot bottom burning, i.e. 3.5 $M_\odot$. Stars with mass below 3.5 $M_\odot$ reach the C-star stage and eject into the interstellar medium gas enriched in carbon, nitrogen and ^{17}O. The higher mass counterparts evolve at large luminosities, between 3×10^4 and 10^5 $L_\odot$. The mass expelled from the massive AGB stars shows the imprinting of proton-capture nucleosynthesis, with considerable production of nitrogen and sodium and destruction of ^{12}C and ^{18}O. The comparison with the most recent results from other research groups is discussed, to evaluate the robustness of the present findings. Finally, we compare the models with recent observations of galactic AGB stars, outlining the possibility offered by *Gaia* to shed new light on the evolution properties of this class of objects.

Key words: stars: abundances – stars: AGB and post-AGB – stars: carbon – stars: distances.

1 INTRODUCTION

Stars of mass in the range $1\,M_\odot \leq M \leq 8\,M_\odot$, after the consumption of helium in the core, evolve through the asymptotic giant branch (AGB) phase: above a degenerate core, composed of carbon and oxygen (or of oxygen and neon, in the stars of highest mass), a 3α burning zone and a region with CNO nuclear activity provide alternatively the energy required to support the star (Becker & Iben 1980; Iben 1982; Iben & Renzini 1983; Lattanzio 1986). Because helium burning is activated in condition of thermal instability (Schwarzschild & Harm 1965, 1967), CNO cycling is for most of the time the only active nuclear channel, whereas ignition of helium occurs periodically, during rapid events, known as thermal pulses (TP).

Though the duration of the AGB phase is extremely short when compared to the evolutionary time of the star, it proves of paramount importance for the feedback of these stars on the host environment. This is because it is during the AGB evolution that intermediate-mass stars lose their external mantle, thus contributing to the gas pollution of the interstellar medium. In addition, these stars have been recognized as important manufacturers of dust, owing to the thermodynamic conditions of their winds, which are a favourable environment to the condensation of gas molecules into solid particles (Gail & Sedlmayr 1999).

For the above reasons, AGB stars are believed to play a crucial role in several astrophysical contexts.

On a pure stellar evolution side, they are an ideal laboratory to test stellar evolution theories, because of the complexity of their internal structure. In the context of the Galaxy evolution, the importance of AGB stars for the determination of the chemical trends traced by stars in different parts of the Milky Way has been recognized in several studies (Romano et al. 2010; Kobayashi, Karakas & Umeda 2011). Still in the Milky Way environment, massive AGB stars have been proposed as the main actors in the formation of multiple populations in globular clusters (Ventura et al. 2001). Moving out to the Galaxy, it is generally believed that AGB stars give an important contribution to the dust present at high redshift (Valiante et al. 2009, 2011); furthermore, these stars play a crucial role in the formation and evolution of galaxies (Santini et al. 2014).

It is for these reasons that the research on AGB stars has attracted the interests of the astrophysical community in the last decades.

The description of these stars is extremely difficult, owing to the very short time steps (of the order of one day) required to describe the TP phases, which leads to very long computation times. Furthermore, the evolutionary properties of these stars are determined by the delicate interface between the degenerate core and the tenuous, expanded envelope, thus rendering the results obtained extremely sensitive to convection modelling (Herwig 2005; Karakas & Lattanzio 2014).

There are two mechanisms potentially able to alter the surface chemical composition, namely hot bottom burning (hereinafter

⋆ E-mail: dicrisci@gmail.com

HBB) and third dredge-up (TDU). The efficiency of the two mechanisms potentially able to alter the surface chemical composition, namely HBB and TDU, depends critically on the method used to determine the temperature gradients in regions unstable to convective motions (Ventura & D'Antona 2005a) and on the details of the treatment of the convective borders, for what concerns the base of the convective envelope and the boundaries of the shell that forms in conjunction with each TP, the so-called 'pulse-driven convective shell'. The description of mass-loss also plays an important role in the determination of the evolutionary time-scales (Ventura & D'Antona 2005b; Doherty et al. 2014).

Given the poor knowledge of some of the macro-physics input necessary to build the evolutionary sequences, primarily convection and mass-loss, the comparison with the observations is at the moment the only way to improve the robustness of the results obtained.

On this side, the Magellanic Clouds have been so far used much more extensively than the Milky Way (Groenewegen & de Jong 1993; Marigo, Girardi & Bressan 1999; Karakas, Lattanzio & Pols 2002; Izzard et al. 2004; Stancliffe, Izzard & Tout 2005; Marigo & Girardi 2007), given the unknown distances of Galactic sources, which render difficult any interpretation of the observations. Very recent works outline the possibility of calibrating AGB models based on the observations of the AGB population in dwarf galaxies in the Local Group (Rosenfield et al. 2014, 2016). The attempts of interpreting the observations of metal-poor environments, typical of the Magellanic Clouds and of the galaxies in the Local Group, have so far pushed our attention towards sub-solar AGB models, published in previous works of our group (Ventura & D'Antona 2008, 2009, 2011; Ventura et al. 2013). The main drivers of these researches were the understanding of the presence of multiple populations in globular clusters and the comparison of our predictions with the evolved stellar population of the Magellanic Clouds (Dell'Agli et al. 2015a,b; Ventura et al. 2015, 2016) and metal-poor dwarf galaxies of Local Group (Dell'Agli et al. 2016). The advent of the ESA-*Gaia* mission will open new frontiers in the study of stars of any class, and in particular for the evolved stellar population of the Milky Way. Launched in 2013 December, *Gaia* will allow constructing a catalogue of around more than 1 billion astronomical objects (mostly stars) brighter than 20G mag (where G is the *Gaia* whitelight passband; Jordi et al. 2010), which encompasses ∼1 per cent of the Galactic stellar population. During the 5 year mission lifetime, each object will be observed 70 times on average, for a total of ∼630 photometric measurements in the G band, the exact number of observations depending on the magnitude and position of the object (ecliptic coordinates) and on the stellar density in the object field. *Gaia* will perform μas global astrometry for all the observed objects, thus allowing the determination of the distance of several AGB stars with unprecedented accuracy, refining the parallax determination of all the stars in the *Hipparcos* catalogue and dramatically increasing the number of accurately known parallaxes. The first release of the *Gaia* catalogue is foreseen by the end of summer 2016, and it will contain positions and G-magnitudes for all single objects with good astrometric behaviour. In order to benefit from the possibilities offered by the upcoming *Gaia* data, we calculated new AGB models with solar metallicity, completing our library, so far limited to sub-solar chemical composition models. The main goal of the present work is to explore the possibilities, offered by the comparisons with observations, to further constrain some of the still poorly known phenomena affecting this class of objects. This task is essential to be able to assess the role played by AGB stars in the various contexts discussed earlier in the section.

To this aim, after the presentation of the main physical and chemical properties of the solar chemistry AGB models, we will compare our theoretical results with (a) the models available in the literature, to determine their degree of uncertainty and their robustness and (b) recent observations of galactic AGB. In some cases, we will also discuss how *Gaia* will help discriminating among various possibilities still open at present.

The paper is structured as follows: the description of the input used to build the evolutionary sequences is given in Section 2; in Section 3 we present an overall review of the evolution through the AGB ADD phase; the contamination of the interstellar medium determined by the gas ejected from these stars is discussed in Section 4; Section 5 presents a detailed comparison with two among the most largely used sets of models available in the literature; in Section 6 we test our models against the chemical composition of samples of Galactic AGB stars; the conclusions are given in Section 7.

2 PHYSICAL AND CHEMICAL INPUT

The evolutionary sequences used in this work were calculated with the ATON code; the details of the numerical and physical characteristics of the code are thoroughly documented in Ventura et al. (1998), while the most recent updates are presented in Ventura & D'Antona (2009). The interested reader is addressed to those papers for the details of the input adopted to build the evolutionary sequences. Here we provide the ingredients most relevant for the present analysis.

(i) *Chemical composition.* The models presented here are representative of the solar chemical composition. The metallicity is $Z = 0.017$, with initial helium $Y = 0.28$. The distribution of the different chemical elements in the initial mixture is taken from Grevesse & Sauval (1998).

(ii) *Mass range*. The initial mass values are between 1 and 8 $M_\odot$. We did not consider initial masses below 1.25 $M_\odot$, as their surface chemical composition is contaminated only by the first dredge-up, with scarce modification from TDU and no effects from HBB; the chemistry of the $\leq$1.25 $M_\odot$ model reflects a modest contribution from TDU and never reaches the carbon star stage. On the other hand, stars with initial mass above 8 $M_\odot$ undergo core collapse, thus skipping the AGB phase.

(iii) *Convection.* In regions unstable to convective motions, the temperature gradient is determined via the full spectrum of turbulence (FST) model (Canuto & Mazzitelli 1991). In convective zones where nuclear reactions are active, we couple mixing of chemicals and nuclear burning in a diffusive-like scheme (Cloutmann & Eoll 1976). The overshoot from the convective borders (fixed by the Schwarzschild criterion) is described by an exponential decay of convective velocities; the extent of the overshoot region is determined by the e-folding distance of such a decay, which in pressure scaleheight (H_p) units is given by $\zeta \times H_p$. During the core hydrogen-burning phase of stars of mass $M \geq 1.5\,M_\odot$, we assume an extra mixing from the external border of the convective core, with $\zeta = 0.02$; this is based on the constraint on core overshoot necessary to reproduce the observed width of the main sequences of open clusters, given in Ventura et al. (1998). The same overshoot is applied during the core helium-burning phases of the stars of any mass.

During the AGB phase, we allow extra mixing from the internal border of the envelope and from the boundaries of the pulse-driven convective shell; we use $\zeta = 0.002$, in agreement with the calibration based on the observed luminosity function of carbon stars in the Large Magellanic Cloud, given by Ventura et al. (2014b).

Table 1. AGB evolution properties of solar metallicity models.

$M/M_\odot$	τ_{AGB}	per cent (C_{star})[a]	$L_{max}/L_\odot$	T_{bce}^{max}	λ_{max}[b]	$M_C/M_\odot$	$M_f/M_\odot$
1.25	2.0×10^6	0	7.6×10^3	3.4×10^6	0.28	0.51	0.59
1.5	2.1×10^6	4	8.7×10^3	4.3×10^6	0.32	0.51	0.61
1.75	2.4×10^6	4	9.7×10^3	5.6×10^6	0.39	0.51	0.615
2.0	3.8×10^6	4	9.1×10^3	6.0×10^6	0.46	0.49	0.62
2.25	4.2×10^6	5	1.1×10^4	7.8×10^6	0.48	0.49	0.63
2.5	4.0×10^6	10	1.2×10^4	8.0×10^6	0.62	0.49	0.65
3.0	1.8×10^6	15	1.3×10^4	1.1×10^7	0.81	0.56	0.67
3.5	1.0×10^6	0	2.6×10^4	7.1×10^7	0.58	0.66	0.78
4.0	3.1×10^5	0	3.1×10^4	8.0×10^7	0.32	0.79	0.86
4.5	2.4×10^5	0	3.8×10^4	8.4×10^7	0.27	0.83	0.89
5.0	1.9×10^5	0	4.6×10^4	8.7×10^7	0.23	0.86	0.91
5.5	1.6×10^5	0	5.4×10^4	8.9×10^7	0.21	0.89	0.94
6.0	1.2×10^5	0	6.3×10^4	9.1×10^7	0.18	0.93	0.97
6.5	9.0×10^4	0	7.4×10^4	9.4×10^7	0.13	0.99	1.02
7.0	8.0×10^4	0	8.7×10^4	1.0×10^8	0	1.04	1.08
7.5	6.0×10^4	0	9.5×10^4	1.0×10^8	0	1.14	1.16
8.0	5.0×10^4	0	1.0×10^5	1.1×10^8	0	1.21	1.25

[a]Percentage of the duration of the C-rich phase.
[b]The maximum efficiency of TDU, defined as the ratio between the mass mixed in the surface convection region and the mass processed by CNO burning during the interpulse phase.

(iv) *Mass-loss.* The mass-loss rate for oxygen-rich models is determined via the Blöcker (1995) treatment; the parameter entering the Blöcker (1995)'s recipe was set to $\eta = 0.02$, following Ventura, D'Antona & Mazzitelli (2000). Once the stars reach the C-star stage, we use the description of mass-loss from the Berlin group (Wachter et al. 2002, 2008).

(v) *Opacities.* Radiative opacities are calculated according to the OPAL release, in the version documented by Iglesias & Rogers (1996). The molecular opacities in the low-temperature regime ($T < 10^4$ K) are calculated by means of the AESOPUS tool (Marigo & Aringer 2009). The opacities are constructed to follow the changes of the envelop chemical composition, in particular carbon, nitrogen and oxygen individual abundances.

3 THE EVOLUTION THROUGH THE AGB PHASE

The evolution of stars of low and intermediate mass through the AGB phase is mainly driven by the mass of the degenerate core, which determines the brightness of the star, the time required to lose the external mantle and the relative importance of the two mechanisms potentially able to alter the surface chemical composition, namely HBB and TDU. Exhaustive reviews, with detailed explanations of the most important properties of stars evolving through the AGB and the uncertainties related to their description, were published by Herwig (2005) and Karakas & Lattanzio (2014).

A summary of the main physical properties of the models presented here is reported in Table 1 and in Fig. 1, showing the duration of the AGB phase, the maximum luminosity experienced (L_{max}), the core mass at the beginning and at the end of the AGB phase and the largest temperature reached at the base of the convective envelope (T_{bce}^{max}). In the same figure, we also show the results of lower metallicity models (Ventura et al. 2013, 2014a,b), and solar metallicity models calculated by other research groups (Doherty et al. 2014; Cristallo et al. 2015; Karakas & Lugaro 2016).

All the physical quantities show clear trend with the initial mass (M_{init}); an upturn in the core mass versus M_{init} relationship is found around $\sim 2\,M_\odot$, at the transition between lower mass stars, undergoing the helium flash, and more massive objects, experiencing core helium-burning ignition in conditions of thermal stability.

Both L_{max} versus M_{init} and T_{bce}^{max} versus M_{init} trends outline an abrupt transition occurring for masses slightly above $3\,M_\odot$, consequently to the ignition of HBB. As thoroughly documented in the literature (Ventura & D'Antona 2005a), the occurrence of HBB has a significant impact on the AGB evolution. Stars undergoing HBB evolve to brighter luminosities (Blöcker & Schöenberner 1991) and experience a fast loss of their external mantle; on the chemical side, the surface composition reflects the outcome of the nucleosynthesis experienced at the bottom of the surface convective region. Based on these reasons, in the following we discuss separately the main properties of the stars experiencing HBB and the objects of mass below $3\,M_\odot$.

3.1 Massive AGB stars

Stars with initial mass $3\,M_\odot < M_{init} \leq 8\,M_\odot$ experience HBB at the base of the convective envelope.[1] Within this mass interval, we separate $3\,M_\odot < M_{init} < 6.5\,M_\odot$ stars (which develop a carbon–oxygen core) and $6.5\,M_\odot < M_{init} < 8\,M_\odot$ objects, which (after the carbon ignition in a partially degenerate off-centre zone) develop an oxygen–neon core (Garcia-Berro & Iben 1994; Garcia-Berro, Ritossa & Iben 1997; Siess 2006, 2007, 2009, 2010).

On general grounds, the maximum luminosity reached by stars undergoing HBB evolves to brighter and brighter luminosities during the initial AGB phases, as a consequence of the increase in the core mass; in more advanced phases, the overall luminosity declines, owing to the gradual loss of the external mantle, which provokes a general cooling of the whole external zones, that reduces the efficiency of the CNO activity. This behaviour can be seen in Fig. 2, showing the AGB evolution of the surface luminosity of models of different initial masses; we used the (current) mass of the

[1] This mass range depends on metallicity, i.e. lower-Z stars achieve HBB conditions more easily. The lower mass limit to experience HBB decreases to $\sim 2.5\,M_\odot$ for metallicities below $Z = 4 \times 10^{-3}$.

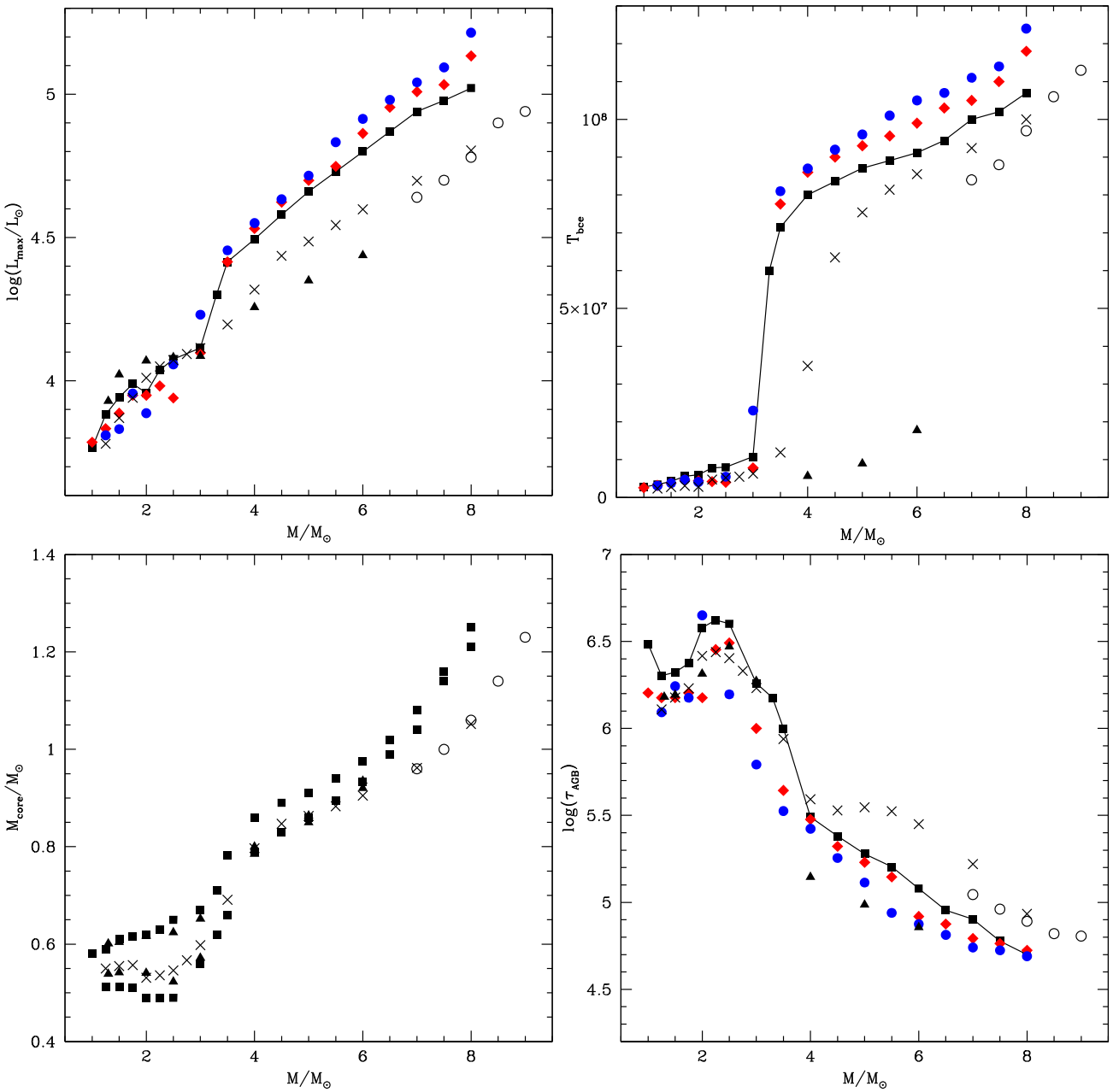

Figure 1. Solar metallicity AGB model properties for various initial masses (filled squares) are presented here. The individual panels show the maximum luminosity reached (top left), the highest temperature experienced at the base of the external mantle (top right), the duration of the TP-AGB phase (bottom right) and the core masses at the beginning and at the end of the AGB evolution (bottom left). The models at $Z = 4 \times 10^{-3}$ and 8×10^{-3} metallicities are indicated, respectively, with blue filled circles and red diamonds. For comparison, we also show the results from Cristallo et al. (2009, 2015, triangles), Karakas & Lugaro (2016, crosses) and Doherty et al. (2014, open circles).

star as abscissa, to allow the simultaneous plot of all the models. As clear from Fig. 2 (see also the top-left panel of Fig. 1), the highest luminosity experienced is extremely sensitive to $M_{\rm init}$, ranging from $\sim$25 000 $L_\odot$ for the $M_{\rm init} = 3.5\,M_\odot$ model to $\sim 10^5$ $L_\odot$ for $M_{\rm init} = 8\,M_\odot$.

The luminosity dependence on initial mass is determined by the larger core masses of larger initial mass models, as shown in the bottom-left panel of Fig. 1. Core masses range from $\sim$0.7 $M_\odot$ ($M_{\rm init} = 3.5\,M_\odot$) to $\sim$1.25 $M_\odot$ ($M_{\rm init} = 8\,M_\odot$). Higher initial mass models experience a faster loss of the external envelop and thus a shorter AGB phase, because larger luminosities imply larger mass-loss rates. While the AGB phase of a 3.5 $M_\odot$ star lasts $\sim 10^6$ yr, in the case of the 8 $M_\odot$ star it is limited to $\sim 5 \times 10^4$ yr (see the bottom-right panel of Fig. 1).[2]

The core mass also affects the temperature at the base of the convective envelope, which, as shown in the top-right panel

[2] A word of caution is needed here: the short duration of the AGB phase of massive AGBs, particularly of the stars whose initial mass is close to the threshold limit to undergo core collapse, is partly due to the steep dependence on luminosity of the mass-loss rate used here (Blöcker 1995); the interested reader can find in Doherty et al. (2014) an exhaustive discussion on this subject.

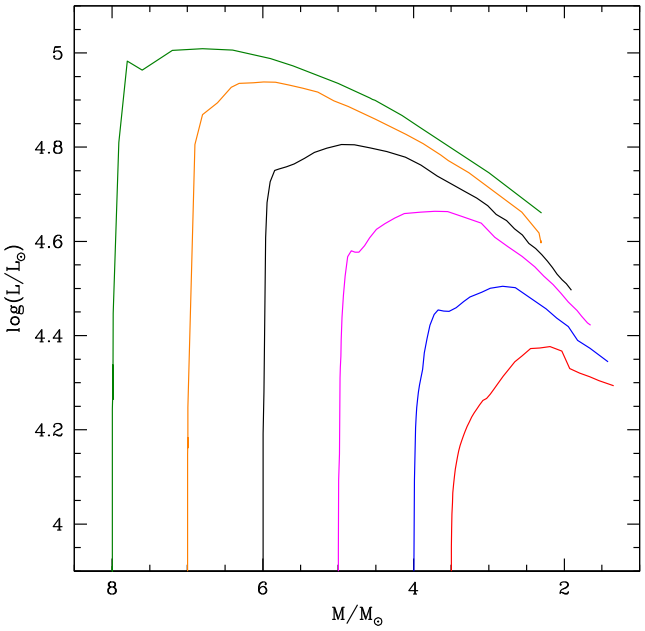

Figure 2. The AGB evolution of the maximum surface luminosity reached by stars of different masses, experiencing HBB. On the abscissa, we report the mass of the star (decreasing during the evolution). The various tracks correspond to model of initial mass 3.5 $M_\odot$ (red), 4 $M_\odot$ (blue), 5 $M_\odot$ (magenta), 6 $M_\odot$ (black), 7 $M_\odot$ (orange) and 8 $M_\odot$ (green).

of Fig. 1, increases linearly with mass, ranging from ∼60 MK ($M_{\rm init} = 3.5\,M_\odot$) to ∼110 MK ($M_{\rm init} = 8\,M_\odot$). Models of higher mass are therefore expected to experience a stronger HBB, with a more advanced nucleosynthesis at the base of the convective envelope.

Fig. 1 allows one to appreciate the effects of metallicity: lower metallicity models reach higher temperatures at the base of the envelope, thus they experience stronger HBB conditions, and their external regions are exposed to a more advanced nucleosynthesis.

The surface chemical composition of massive AGB stars is mainly determined by HBB, with a modest contribution from TDU. The effects of the latter mechanism are more evident towards the latest evolutionary phases, when HBB is turned off by the gradual consumption of the external envelope. In stars of mass around ∼3.5 $M_\odot$, with an initial mass just above the threshold necessary to activate HBB, the evolution of the surface chemistry is given by the balance of the two mechanisms.

3.1.1 *CNO cycling*

Fig. 3 shows the variation with time of the CNO elements' surface mass fraction in stars experiencing HBB. The surface carbon diminishes by ∼30 per cent during the first dredge-up episode and is further destroyed during the AGB phase, since the early TPs. Independently of the initial mass, an equilibrium is reached, where the surface carbon is ∼50 smaller than the initial value and the $^{12}C/^{13}C$ ratio is ∼4; as clearly shown in the figure, most of the mass ejected by these stars has this chemical composition. In the final AGB phases, when HBB is no longer active, some carbon is transported to the surface by TDU; this is particularly evident in the tracks corresponding to 4 and 4.5 $M_\odot$ models. The 3.5 $M_\odot$ star follows a different behaviour, with the AGB evolution divided into three phases: (a) the initial phase, when the surface carbon increases owing to the effects of TDU; (b) an intermediate phase, when HBB destroys the carbon previously accumulated; (c) the final TPs, when HBB is turned off and the surface carbon increases again.

The destruction of the surface carbon is related to the relatively low temperatures required to activate carbon burning at the base of the envelope of AGB stars, namely $T_{\rm bce} \sim 40$ MK; as shown in Fig. 1, these $T_{\rm bce}$'s are reached by all models experiencing HBB during the initial AGB phase. The only exception is the 3.5 $M_\odot$ model, where the temperature necessary to start proton-capture nucleosynthesis by ^{12}C nuclei is reached in more advanced AGB phases, after some TDU episodes occurred (see the left-hand panel of Fig. 3).

The activation of the CNO nucleosynthesis leads to the synthesis of nitrogen, which is increased (see the middle panel of Fig. 3) almost by an order of magnitude at the surface of the stars. It is worth noticing that most of this nitrogen has a secondary origin in the present models, as N is essentially produced by the carbon originally present in the star.

The evolution of surface oxygen abundance is more complicated, as the activation of the whole CNO cycle (with the oxygen destruction) requires temperatures significantly higher than those necessary for the carbon burning ignition, namely ∼80 MK. This makes oxygen depletion extremely sensitive to mass and chemical composition, as these are the two most relevant quantities in the determination of the temperature at which HBB occurs. Ventura et al. (2013) showed that massive AGBs at $Z = 3 \times 10^{-4}$ metallicity produce

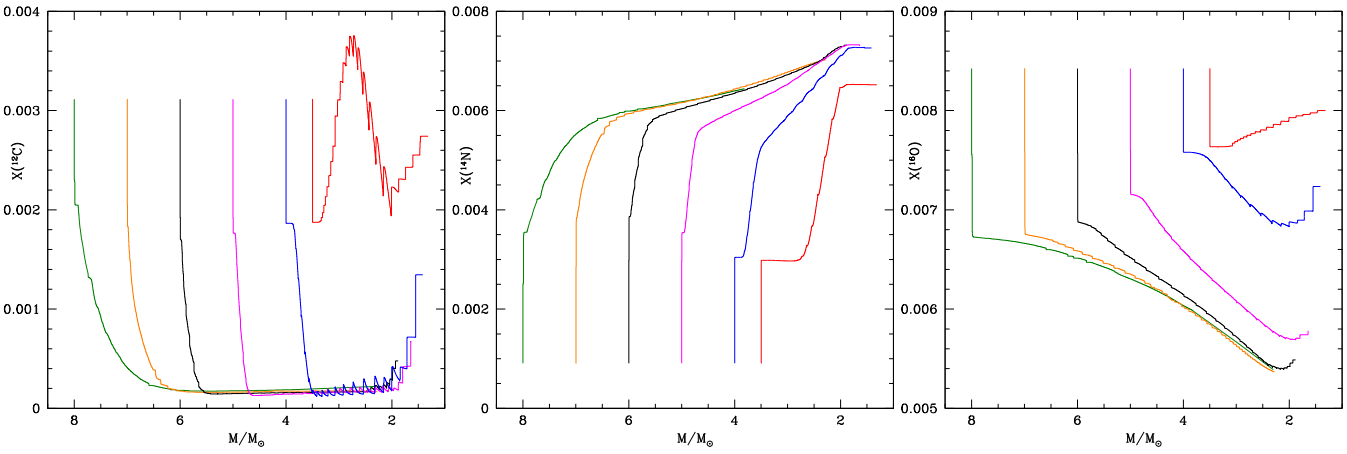

Figure 3. The variation of the surface abundance of ^{12}C (left-hand panel), ^{14}N (middle), ^{16}O (right) during the same AGB models shown in Fig. 2.

ejecta with an oxygen content a factor of 10 smaller compared to the gas from which the stars formed. In contrast, higher metallicity AGBs ($Z = 8 \times 10^{-3}$) were shown to undergo a less advanced nucleosynthesis and to eject gas with an oxygen content on average ∼0.2 smaller than the initial value.

As discussed earlier in this section (see also the top-right panel of Fig. 1), solar metallicity models have a less efficient HBB compared to lower metallicity models. Therefore, the surface oxygen survives more easily in the solar metallicity models. As shown in Fig. 3, the lowest oxygen abundances (∼30–40 per cent below the initial values) are present in the most massive models evolution, in the final AGB phases. For $M_{\rm init} \leq 4\,{\rm M}_{\odot}$, the surface oxygen decreases during the second dredge-up event and is produced during the following AGB phase, owing to the effects of TDU.

Considering oxygen isotopes, the HBB nucleosynthesis is accompanied by a considerable destruction of the surface ^{18}O, which is rapidly consumed starting with the early TPs, when it reaches an equilibrium abundance of $^{18}{\rm O}/^{16}{\rm O} \sim 10^{-6}$. The destruction of ^{18}O occurs at the same temperatures required for carbon burning ignition. In contrast, ^{17}O is produced as soon as ^{16}O burning begins, the overall production factor ranging from 5 to 10, depending on the initial mass of the star. The variation of the $^{18}{\rm O}/^{17}{\rm O}$ ratio of the models discussed here is shown in the right-hand panel of Fig. 11.

3.1.2 *Sodium production*

The Ne–Na nucleosynthesis is activated at the same temperatures at which oxygen burning occurs. The evolution of surface sodium abundance during the AGB phase is complicated (Mowlavi 1999) and depends on the balance between the production channel (i.e. the proton-capture process by ^{22}Ne nuclei) and the destruction reactions [$^{23}{\rm Na}(p,\gamma)^{24}{\rm Mg}$ and $^{23}{\rm Na}(p,\alpha)^{20}{\rm Ne}$ reactions, with the latter providing the dominant contribution]. The production mechanisms prevail at temperatures lower than 90 MK, whereas the destruction reactions, whose cross-sections have a steeper dependence on temperature, become dominant for $T > 90$ MK. At the beginning of the AGB phase, sodium is thus produced via ^{22}Ne burning, whereas it is destroyed in more advanced phases, when the destruction processes predominate (Ventura & D'Antona 2006, 2008).

The variation of the sodium surface abundance during the AGB phase for the solar metallicity models is shown in Fig. 4. The dependence on initial mass offers an interesting example of how the temperature at the base of the convective zone is crucial to determine the nucleosynthesis in these stars. The $T_{\rm bce}$ dependence on $M_{\rm init}$ shown in the top-right panel of Fig. 1 explains the results of Fig. 4. In stars with $M_{\rm init} \geq 6\,{\rm M}_{\odot}$, sodium is produced in the initial AGB phases and partly destroyed later on, when $T_{\rm bce}$ exceeds 90 MK and HBB reaches the strongest efficiency. In stars with $4\,{\rm M}_{\odot} \leq M_{\rm init} < 6\,{\rm M}_{\odot}$, sodium is produced during the whole AGB phase, with no destruction, because the temperature at the base of the external mantle is lower than 90 MK (see the top-right panel of Fig. 1 and Table 1). For stars with initial mass just above the threshold to activate HBB (here represented by the $3.5\,{\rm M}_{\odot}$ star), only a small production of sodium occurs, because the temperature is not high enough to allow an efficient ^{22}Ne burning.

In summary, unlike the stars of lower metallicity (Ventura & D'Antona 2011), here the destruction processes never really predominate, because of the lower temperatures reached at the bottom of the convective envelope. This results into a significant increase in the surface sodium, with final abundances four to five times larger than the initial values. The highest sodium production is reached in the $4\,{\rm M}_{\odot}$ model, because the destruction reactions are never activated during the entire AGB life.

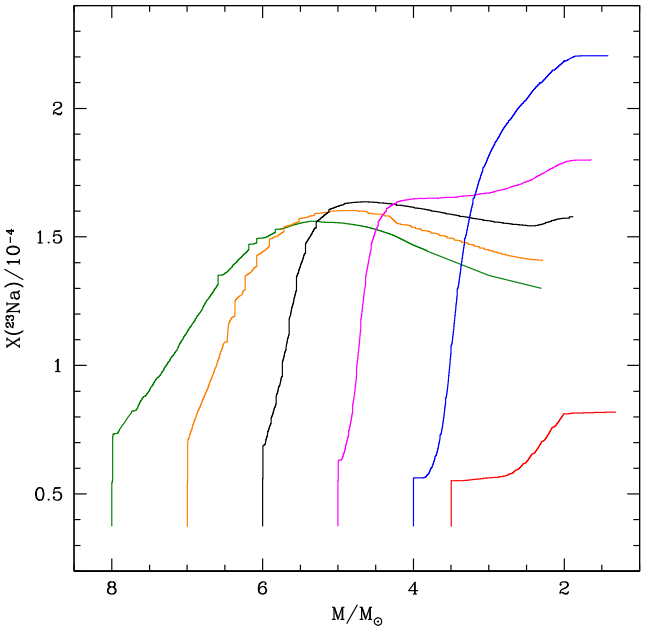

Figure 4. The variation of the surface sodium mass fraction (in 10^{-4} units) of AGB models experiencing HBB. The colour coding is the same as in Fig. 2.

3.1.3 *Mg–Al nucleosynthesis*

The magnesium–aluminium nucleosynthesis is activated at HBB temperatures close to 100 MK: the proton capture by ^{24}Mg nuclei starts a series of reaction, whose outcome is the increase in the surface content of the two heavier isotopes of magnesium and the aluminium synthesis (Arnould, Goriely & Jorissen 1999; Siess & Arnould 2008). Ventura et al. (2013) describe the extreme sensitivity of the Mg–Al nucleosynthesis efficiency to metallicity. As consequence of the different HBB strength at different chemical composition, in low-metallicity stars a significant production of aluminium occurs, whereas in objects with higher metallicities magnesium burning is less efficient, with a more limited aluminium synthesis.

In the present solar metallicity models, the activation the Mg–Al nucleosynthesis is limited to stars with $M_{\rm init} \geq 5\,{\rm M}_{\odot}$. The largest ^{24}Mg depletion ($\delta \log(^{24}{\rm Mg}) \sim -0.15$ dex) is found in the largest initial mass models; in all cases, no significant aluminium synthesis occurs.

3.1.4 *Lithium*

Lithium is synthesized during the AGB phase via the Cameron–Fowler mechanism, which is started by the activation of α capture reactions by ^{3}He nuclei at the base of the surface convective zone (Cameron & Fowler 1971). Sackmann & Boothroyd (1992) showed that the use of a self-consistent coupling between nuclear burning at the base of the envelope and mixing of chemicals in the same region leads to production of great quantities of lithium in the surface layers of AGB stars, provided that a minimum temperature of ∼30 MK is reached at the base of the external mantle. As shown in Fig. 1 and reported in Table 1, this property is shared by all the models presented here, with initial mass $M_{\rm init} \geq 3.5\,{\rm M}_{\odot}$, do reach the required temperature.

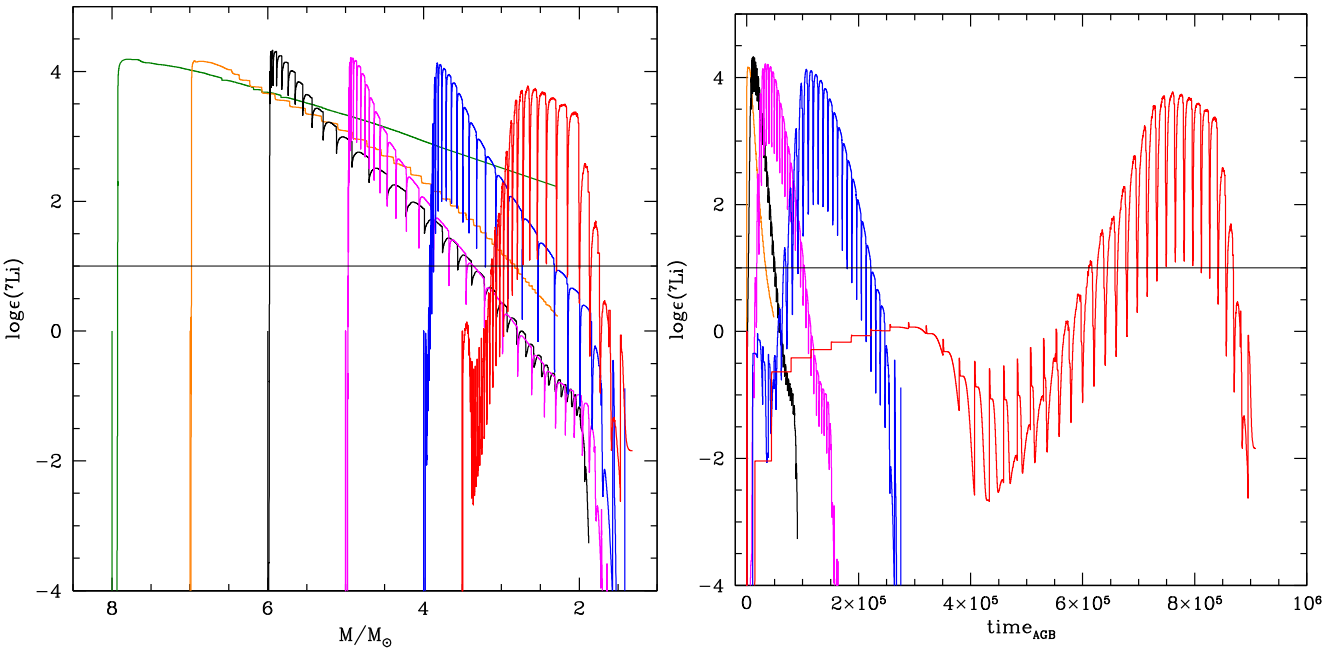

Figure 5. Surface lithium abundance evolution for the same models shown in Fig. 2; the same colour coding is adopted. The quantity on the ordinate is $\log(\epsilon(^7\mathrm{Li}) = \log(^7\mathrm{Li/H}) + 12$. In the left-hand panel, we show the surface lithium as a function of the initial mass, whereas on the right we use the AGB time as abscissa. The horizontal line at $\log(\epsilon(^7\mathrm{Li}) = 1$ indicates the limit above which the stars are considered lithium-rich.

Fig. 5 shows the variation of the surface lithium in our simulated stars during the AGB evolution: the results are shown as a function of the current mass of the stars and of the time counted from the beginning of the AGB phase.

Lithium is produced since the early TP-AGB phases, as soon as HBB is activated. The only exception to this behaviour is the $3.5\,\mathrm{M}_\odot$ model, in which lithium production occurs in more advanced AGB phases, after the star has experienced a C-star phase. In agreement with the general understanding of the lithium production in these objects, the surface lithium reaches a maximum abundance, after which it decreases below any detectability threshold. This apparently anomalous behaviour (the temperature at the base of the envelope keeps increasing until after the surface lithium is consumed, which would further favour the rate at which the Cameron–Fowler mechanism works) is due to the exhaustion of the surface ^{3}He which is at the base of the nuclear chain leading to lithium production.

AGB stars of solar chemical composition are expected to have a longer lithium-rich phase compared to metal-poor AGBs because the smaller temperatures at the base of the envelope (see the top-right panel of Fig. 1) delay the surface ^{3}He exhaustion.

As shown in the right-hand panel of Fig. 5, the lithium-rich phase lasts for about half of the AGB evolution of these stars. The gas yields are therefore expected to show some lithium enrichment.

Stars with initial mass higher than $\sim 7\,\mathrm{M}_\odot$ are expected to be lithium-rich for the whole AGB phase because their large mass-loss rates make the time-scale for envelop consumption comparable to the ^{3}He destruction time-scale. This result must be taken with some caution though, as it is strongly sensitive to the mass-loss mechanism description.

3.2 Low-mass AGB stars

The stars with initial mass below $3.5\,\mathrm{M}_\odot$ do not experience any HBB; thus, their chemical composition is entirely determined by the repeated TDU events that follow each TP. This is going to affect not only their variation of the surface chemistry, but also their physics.

The main quantities related to the evolution of low initial mass AGB stars are shown in Fig. 6, where we report the variation of the luminosity, effective temperature, mass-loss rate and the surface C/O ratio during the AGB phase.

The C/O ratio evolution shows that after each TP some carbon is dredged up to the surface increasing the C/O ratio. Only stars with initial mass greater than $1.5\,\mathrm{M}_\odot$ reach the C-star stage; lower mass stars, while experiencing some carbon enrichment, lose the external mantle before C/O exceeds unity.

Reaching the C-star stage has important effects on the evolution of these objects. As shown in Fig. 6, the external regions of the star undergo a considerable expansion after the C/O ratio grows above unity: the effective temperature drops initially to ∼3500 K and decreases further below 3000 K while the surface carbon abundance increases. This behaviour is a consequence of the formation of CN molecules in C-rich regions, which favours a considerable increase in the opacity and in the mass-loss rates. This effect was predicted in a seminal paper by Marigo (2002) and confirmed in more recent, detailed explorations by Ventura & Marigo (2009, 2010).

As shown in the bottom-left panel of Fig. 6, when stars become carbon-rich, their mass-loss rates increase up to $\sim 2 \times 10^{-4}\,\mathrm{M}_\odot\,\mathrm{yr}^{-1}$ in the very final phases. The increase in the mass-loss rate is due to two different effects: (a) the expanded envelope becomes less and less gravitationally bound, thus overcoming the gravitational pull is easier and (b) the lower effective temperatures favour the formation of large quantities of carbon dust in the wind, which in turn increases the effects of the radiation pressure on the dust particles in the circumstellar envelope.

Given the above, it is clear why the evolutionary time-scales become significantly shorter when stars become C-rich: the envelope is lost rapidly, only a few (if any) additional TDU events can occur to further increase the surface carbon abundance.

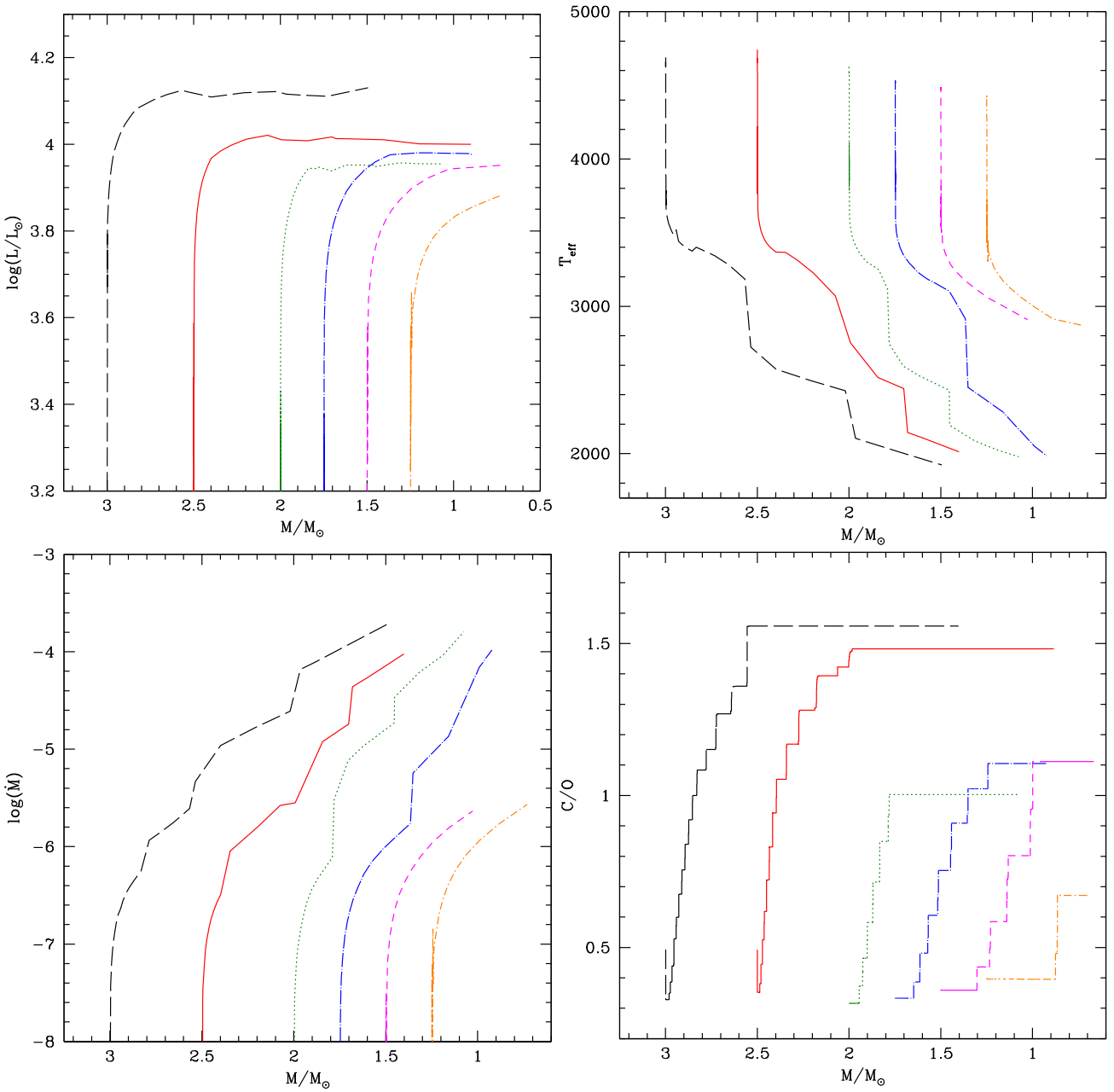

Figure 6. The main physical and chemical properties of low-mass ($M_{\rm init} \leq 3\,{\rm M}_{\odot}$) AGB stars are shown as a function of decreasing initial mass. Individual panels show the behaviour of luminosity (top left), effective temperature (top right), mass-loss rate (bottom left) and C/O ratio (bottom right). The tracks in the panels refer to models of initial mass $1.25\,{\rm M}_{\odot}$ (dotted, short-dashed, orange), $1.5\,{\rm M}_{\odot}$ (short-dashed, magenta), $1.75\,{\rm M}_{\odot}$ (dotted, long-dashed, blue), $2\,{\rm M}_{\odot}$ (dotted, green), $2.5\,{\rm M}_{\odot}$ (solid, red) and $3\,{\rm M}_{\odot}$ (long-dashed, black).

The models with mass close to the threshold required to activate HBB, namely $M_{\rm init} \sim 2.5$–$3\,{\rm M}_{\odot}$, undergo a higher number of TDU events before their mantle is lost. Consequently, they are the stars with the largest relative duration of the C-star phase (∼15 per cent) and with the highest final C/O ratio (C/O ∼ 1.5, see Table 1).

Fig. 7 shows the surface $^{12}{\rm C}/^{13}{\rm C}$ ratio and the luminosity of the models becoming carbon stars during the AGB evolution, as the surface C/O, shown on the abscissa, increases. These results show that carbon stars are expected to evolve at luminosities $8000\,{\rm L}_{\odot} < L < 12\,000\,{\rm L}_{\odot}$. Furthermore, the surface $^{12}{\rm C}/^{13}{\rm C}$ ratio is expected to be above 50.

From the above arguments, we understand that the evolution of the C-rich AGB stars is mainly driven by the surface C/O ratio, the latter quantity affecting directly the rate at which mass-loss occurs, thus the time-scale of this phase.

This is a welcome result for what concerns the robustness of the present findings. The increase in the C/O ratio depends on the treatment of convective borders during each TP, particularly of the assumed extra mixing from the base of the envelope and the boundaries of the pulse-driven convective shell; however, although a deeper overshoot would favour larger carbon abundances, this would be counterbalanced by the increase in the rate of mass-loss, which would lead to an earlier consumption of the stellar mantle, thus reducing the number of additional TDU events.

On the statistical side, it is much more likely to detect a star when it is oxygen-rich than during the C-star phase. On the other hand,

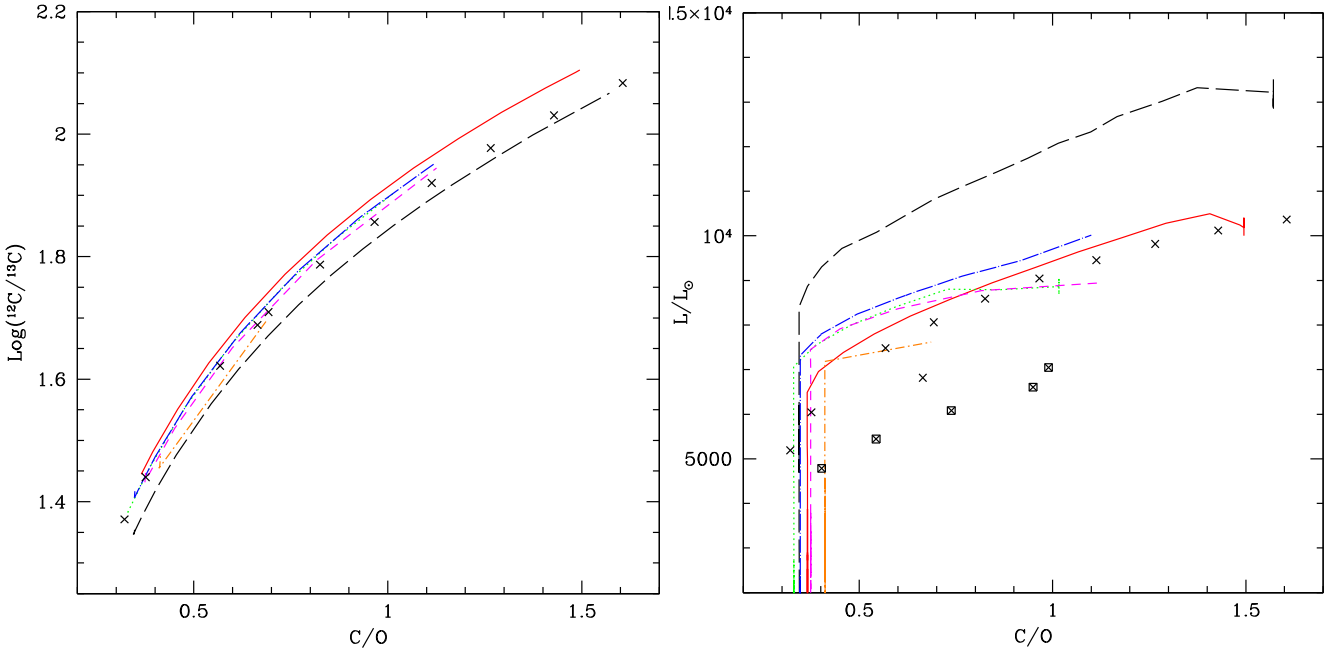

Figure 7. The variation of the surface $^{13}C/^{12}C$ ratio (left-hand panel) and of the luminosity (right) for models with mass $M_{\rm init} \leq 3\,M_{\odot}$ during the AGB phase. The two quantities are shown as a function of the surface C/O ratio. The same colour coding of Fig. 6 was adopted. Crosses and crossed squares refer to C15 models with initial mass 3 and $1.5\,M_{\odot}$, respectively.

as will be discussed in the next section, the latter is much more relevant for the gas and dust pollution determined by these objects, because, as shown in the bottom-right panel of Fig. 6, it is during this phase that most of the mass-loss occurs.

4 GAS POLLUTION

The pollution from AGB stars is determined by the relative importance of HBB and TDU in modifying the surface chemical composition.

When HBB prevails, N-rich and C-poor yields are expected independently from the HBB strength. However, at high temperatures ($T_{\rm bce} > 80$ MK), when the full CNO cycle and the Ne–Na and Mg–Al chains can occur, a modification of the mass fraction of elements heavier than oxygen is also expected. On the other hand, when TDU prevails, C-rich yields are expected with minor contribution from O and N. Table 2 shows the net yields of the various chemical species. The production factor of the CNO elements, defined as the ratio between the average mass fraction of a given element in the ejecta and its initial quantity, is shown in Fig. 8. The left-hand panel refers to ^{12}C, ^{14}N and ^{16}O, whereas on the right we show the less abundant isotopes.

In the low-mass regime ($M \leq 3\,M_{\odot}$), we find production of ^{12}C and ^{14}N. The production factor of both elements increases with the initial mass, up to a maximum of $\sim$3 for $M = 3\,M_{\odot}$. For what concerns carbon, as discussed in Section 3.2, the reason is that higher mass models are exposed to more TDU events and experience a larger enrichment of carbon in the external regions (see the bottom-right panel of Fig. 6). The null production of carbon found in the $1.25\,M_{\odot}$ model stems from the balance between the first dredge-up, after which the surface carbon diminishes, and the following TDUs, which increase ^{12}C in the external regions. The first dredge-up is also responsible for the production of ^{13}C and ^{17}O in low-mass AGB stars (see the right-hand panel of Fig. 8): in the first case, the production factor is $\sim$2.5, fairly independent of $M_{\rm init}$, whereas for the latter isotope it reaches $\sim$10 in the $2\,M_{\odot}$ model. ^{15}N and ^{18}O are practically untouched in these stars.

In the high-mass domain, the effects of HBB take over, changing the above picture substantially. Concerning the elements involved in CNO cycling, the results shown in Fig. 8 can be understood based on the discussion in Section 3.1.1. ^{12}C is found to be 10 times smaller in the ejecta, compared to the initial chemical composition. ^{16}O is also affected by HBB, with a maximum depletion of $\sim$30 per cent. The CNO nucleosynthesis has the effect of synthesizing ^{14}N, which results to be increased by a factor of $\sim$8. The activation of the HBB nucleosynthesis has also the effects of producing ^{13}C and ^{17}O via proton capture by ^{12}C and ^{16}O nuclei. Note that the significant production of ^{17}O (up to a factor of $\sim$10 in the most massive models) is not in contrast with the soft depletion of ^{16}O, given the disparity between the initial abundances of the two elements, which renders a small percentage destruction of ^{16}O sufficient to produce ^{17}O. ^{18}O is severely depleted in the ejecta of these stars, being two to three orders of magnitude smaller than the initial quantity

Turning to Ne–Na elements, the corresponding production factors are shown in the left-hand panel of Fig. 9. We find that ^{22}Ne increases in low-mass stars ($M_{\rm init} \leq 3\,M_{\odot}$), as a consequence of TDU, which brings to the surface matter enriched in ^{22}Ne; similarly to carbon, the production factor of ^{22}Ne is correlated to $M_{\rm init}$, ranging from $f(^{22}Ne) = 2$ for $M_{\rm init} = 1.5\,M_{\odot}$ to $f(^{22}Ne) = 6$ for $M_{\rm init} = 3\,M_{\odot}$. Conversely, sodium is only scarcely touched, in this mass interval.

Like in the case of the CNO elements, the transition to the high-mass domain marks an abrupt change in the surface abundances of the Ne–Na elements, in conjunction with the shift from TDU- to HBB-dominated chemistry. In agreement with the discussion in Section 3.1.2, we find for ^{22}Ne that the ejecta of $M_{\rm init} > 3.5\,M_{\odot}$ exhibit depletion factors ranging from 3 to 10. Note that the trend of $f(^{22}Ne)$ with mass is not monotonic, the most ^{22}Ne-poor ejecta being produced by $M_{\rm init} \sim 6\,M_{\odot}$ models, despite the stronger HBB experienced by their higher mass counterparts. This is motivated by the very large mass-loss rates suffered by 6–8 $M_{\odot}$ stars, which

Table 2. Chemical yields of solar metallicity models.

M	He	^{12}C	^{13}C	^{14}N	^{15}N	^{16}O	^{17}O	^{18}O	^{22}Ne	^{23}Na	^{24}Mg	^{25}Mg	^{26}Mg	^{27}Al
1.25	1.55(−2)	1.15(−4)	3.91(−5)	4.37(−4)	−1.91(−8)	3.70(−5)	2.29(−6)	−1.15(−6)	2.85(−5)	3.59(−7)	0	0	0	0
1.5	2.06(−2)	1.77(−3)	4.81(−5)	8.22(−4)	−3.25(−8)	1.47(−4)	2.59(−6)	−2.82(−6)	1.50(−4)	2.21(−6)	−1.46(−7)	2.08(−6)	1.90(−6)	4.86(−8)
1.75	2.75(−2)	3.26(−3)	5.93(−5)	1.28(−3)	−4.61(−8)	2.55(−4)	1.24(−5)	−4.69(−6)	2.76(−4)	4.07(−6)	−3.66(−7)	4.66(−6)	3.98(−6)	1.44(−7)
2.0	2.00(−2)	4.13(−3)	7.30(−5)	2.02(−3)	−5.56(−8)	3.57(−4)	2.31(−5	−6.53(−7)	3.53(−4)	4.94(−6)	−4.89(−7)	6.15(−6)	5.18(−6)	2.23(−7)
2.25	4.41(−2)	8.23(−3)	8.65(−5)	2.64(−3)	−6.31(−8)	−9.87(−5)	3.50(−5)	−8.19(−6)	7.07(−4)	1.08(−5)	−1.54(−6)	1.88(−5)	1.37(−5)	1.16(−6)
2.5	6.56(−2)	1.09(−2)	8.91(−5)	2.49(−3)	−6.67(−8)	−1.26(−4)	2.66(−5)	−8.36(−6)	9.11(−4)	1.45(−5)	−1.68(−6)	2.18(−5)	1.63(−5)	1.21(−6)
3.0	7.87(−2)	1.38(−2)	1.27(−4)	4.54(−3)	−8.56(−8)	−3.94(−4)	2.92(−5)	−1.25(−5)	1.28(−3)	2.18(−5)	−7.27(−6)	7.71(−5)	4.42(−5)	1.09(−5)
3.5	8.09(−2)	−1.16(−3)	1.15(−3)	1.11(−2)	−2.14(−7)	−1.55(−3)	2.40(−5)	−3.77(−5)	4.00(−4)	9.00(−5)	−1.41(−5)	6.29(−5)	3.88(−5)	3.79(−5)
4.0	9.04(−2)	−7.80(−3)	1.25(−4)	1.67(−2)	−2.88(−7)	−3.93(−3)	3.88(−5)	−5.32(−5)	−2.73(−4)	4.48(−4)	−1.91(−5)	4.36(−5)	1.96(−5)	3.83(−5)
4.5	1.72(−1)	−1.01(−2)	7.60(−5)	1.99(−2)	−3.36(−7)	−6.82(−3)	4.91(−5)	−6.25(−5)	−3.70(−4)	4.74(−4)	−5.39(−5)	4.20(−5)	1.58(−5)	2.78(−5)
5.0	2.59(−1)	−1.18(−2)	6.82(−5)	2.30(−2)	−4.01(−7)	−9.15(−3)	6.07(−5)	−7.13(−5)	−4.51(−4)	5.13(−4)	−1.14(−4)	8.48(−5)	2.91(−5)	1.27(−5)
5.5	3.48(−1)	−1.31(−2)	8.75(−5)	2.61(−2)	−4.40(−7)	−1.10(−2)	7.25(−5)	−7.98(−5)	−5.03(−4)	5.49(−4)	−2.00(−4)	1.63(−4)	3.97(−5)	1.49(−5)
6.0	4.33(−1)	−1.42(−2)	8.71(−5)	2.83(−2)	−4.81(−7)	−1.22(−2)	8.92(−5)	−8.80(−5)	−5.50(−4)	5.80(−4)	−3.05(−4)	2.72(−4)	4.95(−5)	1.88(−5)
6.5	5.17(−1)	−1.60(−2)	8.65(−5)	3.07(−2)	−5.62(−7)	−1.35(−2)	1.09(−4)	−9.62(−5)	−6.11(−4)	6.11(−4)	−4.66(−4)	3.96(−4)	5.62(−5)	1.07(−5)
7.0	5.67(−1)	−1.71(−2)	1.24(−4)	3.27(−2)	−6.54(−7)	−1.45(−2)	1.33(−4)	−1.04(−4)	−6.48(−4)	6.24(−4)	−7.76(−4)	7.11(−4)	3.99(−5)	4.98(−5)
7.5	6.02(−1)	−1.79(−2)	2.13(−4)	3.41(−2)	−8.02(−7)	−1.49(−2)	1.82(−4)	−1.11(−4)	−6.63(−4)	6.42(−4)	−9.12(−4)	9.22(−4)	4.03(−5)	5.12(−5)
8.0	6.34(−1)	−1.89(−2)	2.66(−4)	3.52(−2)	−9.17(−7)	−1.52(−2)	2.06(−4)	−1.17(−4)	−6.88(−4)	6.60(−4)	−1.15(−3)	1.13(−3)	4.10(−5)	5.59(−5)

render the loss of the envelope fast enough to compete with ^{22}Ne destruction.

The reduction of the surface ^{22}Ne favours the production of sodium, which is increased by a factor of 3–5 in the gas expelled from these stars. The most abundant isotope of neon, namely ^{20}Ne, is found to remain practically unchanged in all cases.

Finally, we examine the Mg–Al elements, shown in the right-hand panel of Fig. 9. In the low-mass domain, the surface mass fraction of these elements is only modestly changed; thus, the corresponding production factor is close to unity. In models of higher mass, proton-capture nucleosynthesis occurs, but for the solar metallicity the HBB temperatures are not sufficiently large to allow significant depletion of ^{24}Mg, which is the starting reaction of the whole cycle: as shown in the right-hand panel of Fig. 9, the ^{24}Mg in the ejecta is barely depleted by more than ∼25 per cent, even in the models of highest mass. This partial nucleosynthesis is however sufficient to produce ^{25}Mg, which is found to be increased by a factor of ∼4 in the most massive models.

5 THE ROBUSTNESS OF THE PRESENT GENERATION OF AGB MODELS

The results from AGB evolution modelling are sensitive to the treatment of some physical mechanisms still poorly known from first principles, primarily convection and mass-loss. Additional uncertainties come from the nuclear reactions' cross-sections, though this is going to affect only the details of the chemical composition of the ejecta, because the nuclear rates of the reactions giving the most relevant contribution to the overall energy release are fairly well known (Herwig 2005; Karakas & Lattanzio 2014).

A reliable indicator of the predictive power of the present findings can be obtained by comparing with solar metallicity, AGB models found in the literature. For this purpose, in Fig. 1, reporting the main physical properties of the models presented here, we also show the results from Cristallo et al. (2015), Karakas & Lugaro (2016) and Doherty et al. (2014). In the following, we will refer to the four sets of models, respectively, as ATON, C15, K16 and D14.

In the low-mass regime, the main difference between ATON and C15 and K16 results is that the ATON core masses at the beginning of the AGB phase are slightly smaller; thus, the ATON models evolve at lower luminosities and the AGB phase is longer. The largest difference is found for the 2 $M_\odot$ model, which in the ATON case experiences a maximum luminosity 0.08 dex smaller than C15, and the AGB evolution is two times longer (4 Myr versus 2 Myr). K16 models exhibit an intermediate behaviour in this range of mass.

The most relevant differences are found in the high-mass domain, where HBB effects take over. In the comparison among the highest temperatures reached at the base of the convective envelope, ATON models in the range 4–6 $M_\odot$ attain values of the order of 80–90 MK, whereas in the C15 case we find 10 MK $< T_{\rm bce} <$ 20 MK. The K16 models exhibit temperatures closer to, though smaller than, ATON, covering the range 30 MK $< T_{\rm bce} <$ 80 MK in the same interval of mass. Such a dramatic difference has an immediate effect on the luminosity, which for the ATON models, in the same range of mass, is 30 000 $< L/L_\odot <$ 60 000, whereas in the C15 and K16 cases it is, respectively, 20 000 $< L/L_\odot <$ 30 000 and 20 000 $< L/L_\odot <$ 40 000. Because the core masses at the beginning of the AGB phase are very similar in the three cases (see Fig. 1), the differences outlined above must originate from the different description of the convective instability, particularly for what concerns the efficiency

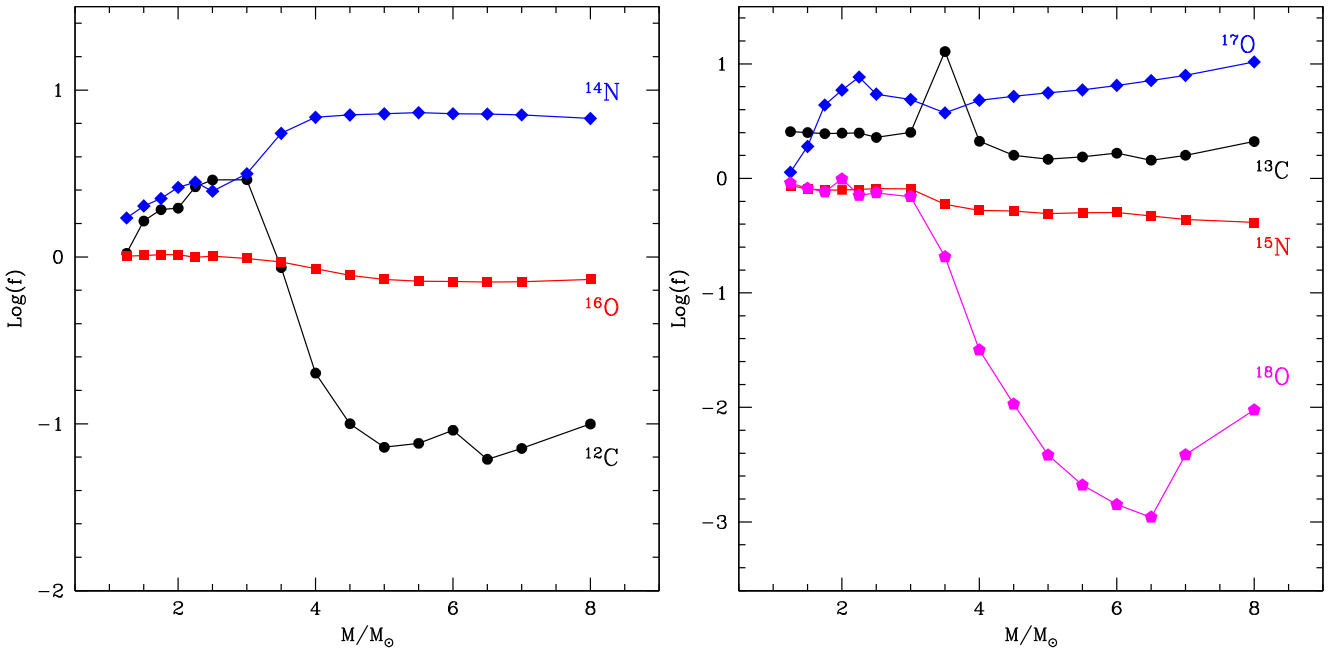

Figure 8. The production factor (see the text for definition) of the CNO isotopes in solar metallicity models. In the left-hand panel, we show the most abundant species, namely ^{12}C (black points), ^{14}N (blue diamonds) and ^{16}O (red squares). The right-hand panel refers to ^{13}C (black points), ^{15}N (red squares), ^{17}O (blue diamonds) and ^{18}O (magenta pentagons).

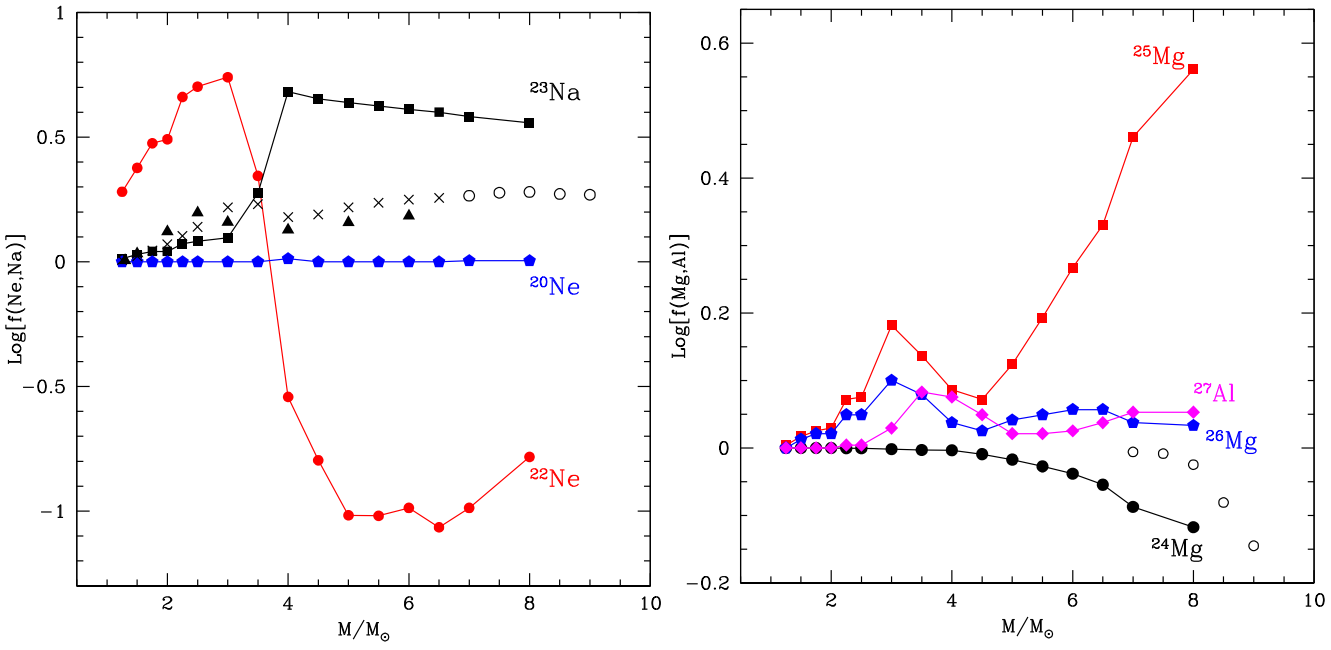

Figure 9. The production factor of the elements involved in the Ne–Na and Mg–Al nucleosynthesis for the models presented here. Left: ^{20}Ne, ^{22}Ne and ^{23}Na are indicated, respectively, with blue pentagons, red points and black squares; the sodium production factor by K16 (crosses), C15 (triangles) and D14 (circles) are also indicated. Right: the production factor of ^{24}Mg (black points), ^{25}Mg (red squares), ^{26}Mg (blue pentagons) and ^{27}Al (magenta diamonds); the results for ^{24}Mg by D14 are indicated with open circles.

of convection in the innermost regions of the envelope. The ATON models are based on the FST treatment (Canuto & Mazzitelli 1991), whereas the C15 and K16 computations used the mixing length theory (MLT) recipe. These results confirm the analysis by Ventura & D'Antona (2005a), who discussed the outstanding impact of convection modelling on the efficiency of HBB experienced by AGB stars.

In the analysis of the behaviour of the core masses, we note that the ATON models present the greatest variation ($\delta M_{\rm C} \sim 0.05\,{\rm M}_{\odot}$) during the whole AGB phase, compared to C15 and K16, for which we have $\delta M_{\rm C} < 0.02\,{\rm M}_{\odot}$: this is due to the deeper penetration of the convective envelope in the phases following each TP in the C15 and K16 cases, which slows the growth of the core during the AGB evolution.

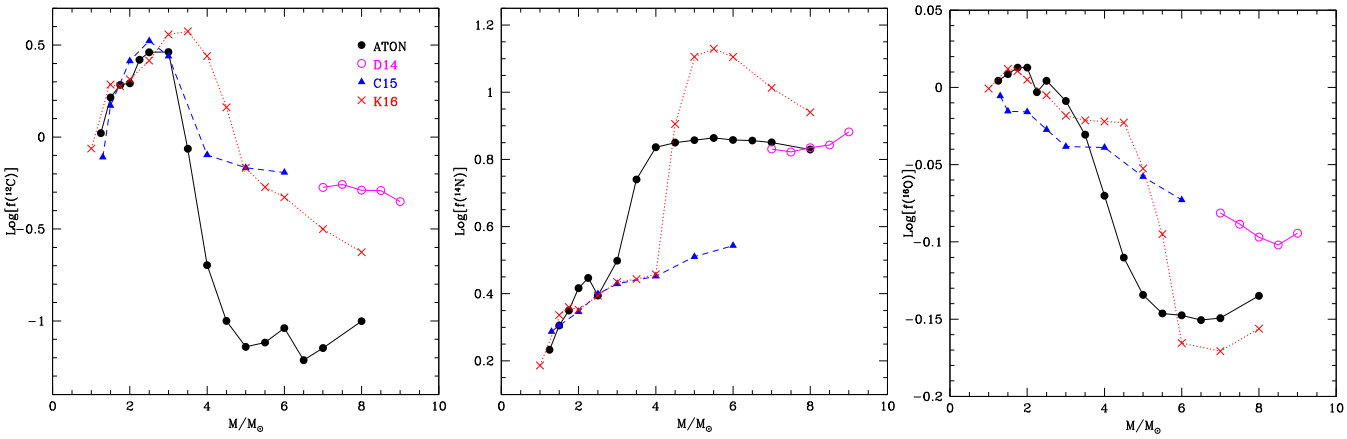

Figure 10. The production factor of ^{12}C, ^{14}N and ^{16}O of the models presented here (shown as black, filled points), compared with results from Cristallo et al. (2015, blue triangles), Karakas & Lugaro (2016, red crosses) and Doherty et al. (2014, magenta circles).

We now focus on the evolution properties of those stars that develop a core made up of oxygen and neon, i.e. those of initial mass above 6.5 $M_\odot$. In this case, we compare the ATON models with D14 and with the 8 $M_\odot$ model by K16.[3] The same initial mass does not correspond to the same core mass during the early AGB phases, because in the ATON case a larger extra mixing from the border of the convective core during the H-burning phase was adopted, which results into a higher core mass at the beginning of the AGB phase. Taking into account this difference, we note that the values of the temperature at the base of the envelope and of the luminosity are similar in the ATON, D14 and K16 cases, whereas the D14 and K16 AGB evolutionary times are longer than ATON. The results from this comparison find an explanation in the different modalities with which convection and mass-loss are described. ATON models are based on a more efficient description of convection (FST, against the MLT treatment used by D14 and K16), which favours larger luminosities and HBB strength; however, ATON models also suffer a very strong mass-loss, which provokes a fast loss of the external mantle, accompanied by a general cooling of the whole external regions, which acts against the achievement of very large HBB temperatures. The longer duration of the AGB phase found in the D14 and K16 models is due to the smaller mass-loss rate adopted compared to ATON. The interested reader may find in D14 an exhaustive discussion of the impact of the mass-loss description on the duration of the TP phase of super-AGB stars.

The differences discussed above have important effects on the yields expected from these stars, which show some differences among the results published by the different research groups.

In Fig. 10, we compare the production factors of the most abundant isotopes involved in CNO nucleosynthesis.

In the low-mass domain, we find that the results concerning carbon are very similar. In all cases, we find a positive trend of the carbon in the ejecta with the stellar mass, as higher mass stars experience more TDU events. ATON, C15 and K16 results are also similar on quantitative grounds, the largest ^{12}C enhancement being ∼3, reached by ∼3 $M_\odot$ models.

[3] The ATON and K16 models of, respectively, 7 and 8 $M_\odot$, produce indeed a hybrid O–Ne core: they undergo an off-centre ignition of carbon, but the temperatures are not sufficient for the convective flame that develops to reach the centre of the star.

The N-production factors of ATON, C15 and K16 are also similar: $f(N)$ increases with the stellar mass, up to $f(N) \sim 3$ for the ∼3 $M_\odot$ models.

In the same range of mass, a few differences are found for what regards oxygen. In the ATON and K16 cases, some oxygen enrichment occurs, whereas no ^{16}O production is found in C15 models.

For what concerns stars of mass above 3 $M_\odot$, the predictions are considerably different. In the ATON case, carbon in the ejecta is severely reduced, almost by a factor of 10. In the C15 and K16 models, this reduction is much smaller, at most by a factor of 4 in the 8 $M_\odot$, K16 model. The results from D14 also predict reduction factors not higher than 2.

Concerning nitrogen, in the mass range $3\,M_\odot < M < 4\,M_\odot$, the ATON models produce more nitrogen, owing to the effects of HBB, not found in the C15 and K16 models of the same mass. In the ATON case, for massive stars, great amount of nitrogen is produced, with production factors in the range 6–8. This behaviour is shared by the D14 models. Conversely, the N-production factor is significantly smaller in the C15 case, where the production factor never exceeds ∼4. The largest production of nitrogen is found in the 5–6 $M_\odot$ models by Karakas & Lugaro (2016): this is due to the combined effects of TDU, which increases the surface carbon, and HBB, which converts the dredge-up carbon into nitrogen.

In the large-mass domain ^{16}O is only modestly reduced in C15 models, whereas in the ATON case the depletion factor in $M_{\rm init} \geq 5\,M_\odot$ models is ∼70 per cent. The comparison between the ATON and K16 models is more tricky: for $M_{\rm init} < 6\,M_\odot$ the ATON models predict more oxygen-poor ejecta, whereas in the range of mass $6\,M_\odot < M < 8\,M_\odot$ the oxygen depletion is slightly higher in the K16 case. In the D14 models, some oxygen depletion is found, though limited to ∼20 per cent.

Turning to sodium, in the large-mass domain, the results are significantly different, as can be seen in the left-hand panel of Fig. 9: in the ATON case, a great production of sodium is expected, the average Na in the ejecta being increased, with respect to the original chemistry, by a factor ranging from 3 to 5. In the K16 and D14 models, the production factor is below 2, whereas in the C15 case it is slightly smaller.

In the range of masses experiencing HBB, the extent of the Mg–Al nucleosynthesis is also model dependent, as shown in the right-hand panel of Fig. 9. The ATON models achieve some processing of ^{24}Mg, which is depleted by at most ∼40 per cent in the most massive case. This is in fair agreement with the results from D14,

whereas in the C15 and K16 models processing of magnesium is negligible.

The differences in the expected chemical enrichment of the interstellar medium can be understood on the basis of the physical input used by the various research groups to calculate the evolutionary sequences. Convection is by far the biggest villain here, determining most of the differences found.

In the low-mass domain, the slight increase in the ^{16}O content found in the ATON and K16 models is due to the adoption of some overshoot from the base of the pulse-driven convective shell, which further enhances the strength of the pulse and, more important, makes the internal regions of the convective envelope to be mixed with more internal zones touched by helium burning, with a higher oxygen content. In the same range of mass, we find that the largest production factor of ^{12}C is similar in the ATON, C15 and K16 cases, indicating that those models experience TDU events of similar depth.

For masses above $3\,M_{\odot}$, the main reason for the differences among the various models is the strength of HBB and the description of mass-loss. The large HBB temperatures are the main actors in the considerable depletion of carbon and production of nitrogen in the ATON models. The K16 models of mass above $5\,M_{\odot}$ and the D14 models produce ejecta with nitrogen enhancement similar to ATON (see the middle panel of Fig. 10), despite that the carbon depletion is more reduced (left-hand panel of the same figure). This is motivated by some TDU events active in the latter models, which transport to the external regions some carbon produced in the helium-burning shell, which is later converted into nitrogen: in summary, while the nitrogen produced in the ATON models is entirely of secondary origin, part of the nitrogen synthesized in the K16 and D14 cases has also a primary component. The best indicator of the efficiency of HBB is the behaviour of oxygen, which is depleted in the ejecta of the ATON and in some K16 models, whereas it is only scarcely touched in the C15 and D14 cases (see the right-hand panel of Fig. 10). Understanding the differences among the ATON and K16 results is not straightforward though. For $M_{\rm init} < 6\,M_{\odot}$, the ATON models predict more oxygen-poor ejecta, because the K16 models are cooler at the base of the envelope (see the top-right panel of Fig. 1); thus, the latter is exposed to a less advanced nucleosynthesis. In the range of mass $6\,M_{\odot} < M < 8\,M_{\odot}$, the oxygen depletion is slightly higher in the K16 case, compared to ATON, despite that the latter models evolve at larger $T_{\rm bce}$'s. The reason for this apparently anomalous behaviour is once more in the large mass-loss rates experienced by the ATON models, which makes the envelope to be lost before a great depletion of the surface oxygen may have occurred.

The efficiency of HBB is also the main factor determining the extent of the Ne–Na and Mg–Al nucleosynthesis experienced. The great enhancement of sodium found in the ejecta of $M \geq 3.5\,M_{\odot}$ ATON models is originated by the large HBB temperatures reached; conversely, in the other cases, the temperatures required to activate the Ne–Na nucleosynthesis are barely reached, which determined a much smaller production of sodium (see the left-hand panel of Fig. 9).

6 INTERPRETATION OF OBSERVED GALACTIC AGB STARS

The discussion of the previous sections outlines how far we are from a full understanding of the main evolutionary properties of AGB stars. The significant differences found between the present models and those by K16, C15 and D14 stress the importance of comparing the expectations from the models with the observations. As a first step towards this direction, we compare the most recent estimates of the CNO elemental and isotopic abundances in Galactic (solar metallicity) AGB stars with the ATON models presented here.

6.1 Extreme O-rich, AGB stars observed by *Herschel*

Justtanont et al. (2013) published *Herschel Space Observatory* (*Herschel* hereafter) observations of five visually obscured OH/IR stars,[4] using CO as a tracer of the thermodynamical structure of the circumstellar envelope. The combination with ground data allowed the determination of the dynamical and dust properties of the wind, and the derivation of the oxygen and carbon isotopic ratios.

To allow a clearer interpretation of the chemical composition of the stars in this sample, we show in Fig. 11 the evolution of the surface ^{12}C/^{13}C (left-hand panel) and of ^{18}O/^{17}O (right), the same models shown in Figs 1 and 3. In all cases, we see a significant reduction of the surface ^{12}C/^{13}C as soon as HBB begins, owing to the destruction of ^{12}C and the synthesis of ^{13}C; eventually, the equilibrium value, ^{12}C/^{13}C ~ 4, is reached. The activation of HBB also determines the destruction of the surface ^{18}O and the synthesis of ^{17}O: the surface ^{18}O/^{17}O is dramatically reduced compared to the initial value, ^{18}O/^{17}O $= 5$. In the models of initial mass $M_{\rm init} \sim 4\,M_{\odot}$, the surface ^{12}C/^{13}C rises again in the final evolutionary phases, after HBB was switched off: under the effects of a few late TDU events, carbon ratios ^{12}C/^{13}C ~ 20 are expected.

The surface chemistry of OH 127.8+0.0 and OH 30.1−0.7 shows the clear imprinting of HBB, with ^{12}C/^{13}C $\sim$ 3–5 and ^{18}O below the detectability threshold. As shown in Fig. 11, this is a common feature of all the models experiencing HBB. The ignition of ^{12}C burning (with consequent synthesis of ^{13}C) and the depletion of ^{18}O are active since the early AGB phases; as shown in Fig. 1, these temperatures at the base of the convective envelope are reached in all the models experiencing HBB. The surface chemistry observed in OH 127.8+0.0 and OH 30.1−0.7 is a common feature of all the models of initial mass $M_{\rm init} \geq 3.5\,M_{\odot}$, thus not allowing us to discriminate among the possible progenitors. The upper limits for the ^{18}O/^{17}O ($\leq$0.1) given by Justtanont et al. (2013) also support our interpretation of these stars being massive HBB stars. Our interpretation agrees with the Justtanont et al. (2013) conclusion of these stars being HBB-AGB stars; the difference in the progenitor mass range [Justtanont et al. (2013) assume masses above $\sim 5\,M_{\odot}$] is just because the minimum mass to activate HBB is model dependent; for example it is $\sim 3.5\,M_{\odot}$ in the ATON models, while it is $\sim 4.5\,M_{\odot}$ in the D14-like models used by Justtanont et al. (2013). We note, however, that these stars might be in a very advanced evolutionary stage, thus implying that their current mass could in principle be significantly smaller (down to $\sim 1\,M_{\odot}$) than the initial mass.

Based on *ISO* spectra and *IRAS* photometry, the SED of these two stars shows up the silicate absorption feature at 9.7 μm, in agreement with the hypothesis that they are undergoing HBB: indeed Dell'Agli et al. (2014) showed that large dust formation occurs in $M_{\rm init} > 3\,M_{\odot}$ stars during the HBB phase. The results by Dell'Agli et al. (2014) were based on models with sub-solar chemical composition; while the dust production by the present models will be addressed in a forthcoming paper, we may anticipate that the conclusions by Dell'Agli et al. (2014) can be safely extended to the

[4] These stars are obscured in the optical range (e.g. García-Hernández et al. 2007) and they are expected to be the more massive AGB stars, experiencing extreme mass-loss rates.

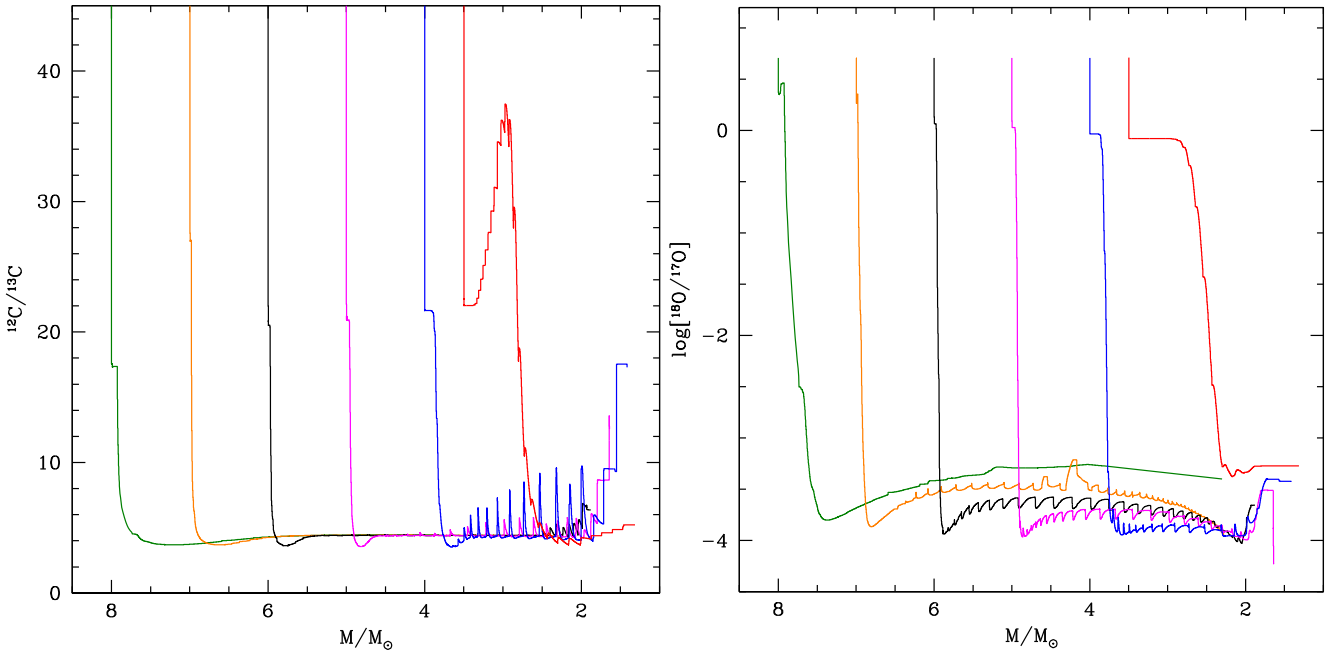

Figure 11. The evolution of the surface $^{12}C/^{13}C$ (left-hand panel) and $^{18}O/^{17}O$ ratios, in the same models shown in Fig. 2. The same colour coding is adopted.

present case, because the larger availability of silicon in the surface regions will further increase dust production in solar metallicity stars. We conclude that OH 127.8+0.0 and OH 30.1−0.7 are evolving through the AGB phases during which HBB is strongest, when dust production is large and the stars lose mass at high rates.

A significant support towards the identification of the precursors of OH 127.8+0.0 and OH 30.1−0.7 could be obtained by the knowledge of their distance, which would allow the determination of their luminosity. This is because, while undistinguishable on the basis of the surface isotopic ratios of carbon and oxygen, the stars of the various masses evolve at different luminosities during the AGB phase. This is clearly shown in Fig. 2, where the range of the luminosities of the various tracks is seen to vary substantially with the initial mass of the star: a luminosity $L \sim 2 \times 10^4\,L_\odot$ would point in favour of the progeny of $\sim$3.5 $M_\odot$ star, whereas a higher mass progenitor, $\sim$8 $M_\odot$, would require much higher luminosities, of the order of $L \sim 10^5\,L_\odot$. It goes without saying that we mentioned only the two extreme cases, neglecting a number of intermediate situations.

The surface chemical composition of AFGL 5379 and OH 26.5+0.6 indicates depletion of ^{18}O, as confirmed by the non-detection of the $H_2^{18}O$ line in the spectra. Unlike the two previous stars, the isotopic carbon ratio, $^{12}C/^{13}C \sim$ 15–20, is significantly higher than the equilibrium value.

A possible interpretation of these data is that AFGL 5379 and OH 26.5+0.6 descend from 3.5–4 $M_\odot$ progenitors and are in the phases following the ignition of HBB, when carbon burning started, but there was no time to reach the equilibrium value. In this case, we expect that the current masses of the stars are close to the initial masses and that the stars are actually lithium-rich.[5] We believe this possibility unlikely, for the following reasons: (a) at the ignition of HBB, these stars would evolve at effective temperatures $T_{\rm eff} \sim 3000$ K, significantly higher than the temperatures deduced by Justtanont et al. (2013), which are slightly above 2000 K; (b) during the same phase, we find that these stars have radii of the order of $\sim$500 $R_\odot$, $\sim$40 per cent smaller than found by Justtanont et al. (2013); (c) the mass-loss rates in the initial HBB phases are at most a few $10^{-6}\,\dot{M}$ yr^{-1}, whereas AFGL 5379 and OH 26.5+0.6 are currently losing mass with rates much higher than $10^{-5}\,\dot{M}$ yr^{-1}.

Our favourite interpretation is that AFGL 5379 and OH 26.5+0.6 are the progeny of $\sim$4 $M_\odot$ stars, and are currently evolving during the final AGB phases. The observed $^{12}C/^{13}C$ is larger than the equilibrium value, because HBB is switched off when the mass of the envelope drops below $\sim$1 $M_\odot$ and a few TDU events are sufficient to increase the surface ^{12}C, thus lifting the $^{12}C/^{13}C$ ratio (see the left-hand panel of Fig. 11). The effective temperatures during the late AGB phases are $T_{\rm eff} \sim 2500$ K, in better agreement with those indicated by the authors, i.e. $T_{\rm eff} \sim 2200$ K. An additional point in favour of this hypothesis is that the radius of the star is expected to be $\sim$800 $R_\odot$, very close to the values proposed by Justtanont et al. (2013). A last argument supporting this conclusion is that the SED of these stars show up a deep silicate feature, suggesting the presence of significant quantities of dust, as expected based on the low temperatures of the models, favouring dust formation. Interestingly, if this hypothesis proves correct, it is possible to constrain the current mass and the luminosity of AFGL 5379 and OH 26.5+0.6: in the final AGB phases of $\sim$4 $M_\odot$ stars, the mass is reduced to 1–2 $M_\odot$ and the luminosity is $L = 2$–$3 \times 10^4\,L_\odot$.

This could be confirmed by an accurate determination of the distances which is not yet available, at the moment, for this type of stars.

Among the stars observed by Justtanont et al. (2013), WXPsc is the least obscured and is still visible in the optical. The carbon ratio for this star is $^{12}C/^{13}C = 10 \pm 4$; this is not highly significant, as it ranges from the values typical of CNO equilibria to those of incomplete CN burning. The information on the $^{18}O/^{17}O$ ratio is hard to interpret: Justtanont et al. (2012) give $^{18}O/^{17}O \sim 1.5$, at odds with the results derived by Justtanont et al. (2013) in a larger sample of extreme OH/IR stars, where they found an upper

[5] This information is however of little help because, as we noted above, these sources are completely obscured in the optical (García-Hernández et al. 2007), leaving no chances of any reliable lithium measurement.

limit for the oxygen isotope ratio of the order of 0.1. Additional information on this star is that the optical spectrum displays a strong Rb line at 7800 Å (Garcia-Hernández, private communication), which suggests that it has already experienced some TPs and TDU episodes, and it is Rb-rich. Confirmation of the $^{18}O/^{17}O$ given by Justtanont et al. (2012) would rule out any contamination from HBB; in this case, the most likely possibility is that WXPsc descends from a progenitor of mass just above the threshold required to activate HBB ($M_{\rm init} \sim 3.5\,M_\odot$) and has already experienced some TDU events, whereas HBB has not yet started.

This interpretation has some problems though, mainly related to the degree of obscuration of the star ($\tau_{10} = 3$, according to Ramstedt & Olofsson 2014), as witnessed by the silicate feature, which is about to be converted into absorption, owing to the increasing thickness of the circumstellar shell: this evidence would rather indicate that WXPsc is evolving through the final AGB phases and is surrounded by great quantities of silicate dust. If this understanding is correct, the surface chemistry of the star should display pieces of evidence of HBB, which seems in contrast with the large $^{18}O/^{17}O$ given by Justtanont et al. (2012). On the other hand, Justtanont et al. (2013) mentioned that there were problems with the observations and analysis of WXPsc, related to possible asymmetries of the circumstellar shell, which may alter their result. In conclusion, any definite interpretation of the evolutionary history of this star will be possible only when a more robust determination of the oxygen isotopic ratio will be available.

6.2 Lithium abundances in O-rich AGB stars

García-Hernández et al. (2007) presented results from high-resolution spectroscopy of a large sample of O-rich AGB stars, for which the lithium and zirconium abundances were measured. The latter element increases under the effects of TDU; thus, its content can be used as a reliable indicator of the efficiency of TDU in the stars observed.

Among the sources observed by García-Hernández et al. (2007), 25 show evidence of lithium, with $\log\epsilon(^7{\rm Li}) > 0.5$, whereas in 32 of them the lithium line was not detected, thus indicating that $\log\epsilon(^7{\rm Li}) < -1$. The distribution of the periods observed is 350–1200 d for lithium-rich objects, whereas the AGB stars with no lithium have periods below 500 d, with the single exception of IRAS 18050−2213, which has a period of 732 d.

The lithium-rich stars in the García-Hernández et al. (2007) sample are interpreted as the progeny of $M_{\rm init} \geq 3.5\,M_\odot$ stars, currently evolving through the lithium-rich phase, when the Cameron–Fowler mechanism is active. Based on the discussion in Section 3.1.4, we know that this phase extends for about half of the AGB evolution of stars of solar metallicity. While on general grounds we cannot identify the mass of the progenitors, statistical arguments suggest that most of the lithium-rich stars descend from 4–5 $M_\odot$ stars. As shown in the right-hand panel of Fig. 5, the lower the mass of the progenitors, the longer the duration of the lithium-rich phase: it is 1.6×10^5 yr for $M = 4\,M_\odot$, 8×10^4 yr for $M = 5\,M_\odot$ and 4×10^4 yr for $M = 6\,M_\odot$. Given these time-scales and the functional form of any realistic mass function, we deduce that the stars observed likely descend from progenitors of mass below 5 $M_\odot$, and have current masses between 2 and 5 $M_\odot$.

The distribution of the periods of the stars in the sample by García-Hernández et al. (2007) further supports this interpretation. The stars with no lithium are either stars of mass below 3.5 $M_\odot$, which do not experience any HBB, or more massive objects in the initial AGB phases, before the Cameron–Fowler mechanism is activated: during these early TP-AGB phases, the stars are more compact and less luminous; thus, their periods are shorter. This is fully consistent with one of the main results of the García-Hernández et al. (2007) analysis, i.e. lithium-rich stars have larger periods than their lithium-rich counterparts. The lack of any strong s-process enrichment in the lithium-rich stars observed by García-Hernández et al. (2007), as deduced by the absence of significant zirconium enrichment, further supports our models. Indeed, this is in agreement with our results, that TDU is scarcely efficient in solar metallicity, massive AGB stars (see the values of λ reported in Table 1).

A final comment concerns the luminosities of lithium-rich stars. Because the ignition of the Cameron–Fowler mechanism requires a minimum temperature at the bottom of the envelope $T_{\rm bce} \sim 30$ MK, this reflects into a minimum luminosity $L = 1.8 \times 10^4\,L_\odot$, i.e. $M_{\rm bol} = -5.88$; this stems from the tight relationship between $T_{\rm bce}$ and L. We note that, although Galactic massive HBB-AGB stars may display strongly variable luminosities and their distances are unknown (García-Hernández et al. 2007), similar truly massive HBB-AGB stars in the Magellanic Clouds consistently display extremely high luminosities of $M_{\rm bol} < -6$ (García-Hernández et al. 2009).

6.3 C isotopes in different types of AGB stars from radio transitions

The group of Galactic AGB stars by Ramstedt & Olofsson (2014) are the most complete sample presented so far, with $^{12}C/^{13}C$ ratios available for stars in different phases of the AGB evolution. This sample includes both carbon stars and oxygen-rich objects. The results are based on radiative transfer modelling of the observed ^{12}CO and ^{13}CO radio transitions; the solution of the energy balance equation allowed the determination of the circumstellar $^{12}CO/^{13}CO$, the rate of mass-loss and the expansion velocity. This information can be used to constrain the evolutionary models.

Before entering the discussion, we believe that it is important to stress at this point that the observational data in the optical/near-IR are more representative of the photosphere, while the radio data, such as those presented in this section, trace the chemistry of the circumstellar envelope. This is confirmed by recent results, showing that in some cases both values do not agree (e.g. Vlemmings et al. 2013). Furthermore, the interpretation of the radio data is subject to several assumptions and modelling. Typically, it is assumed that the radio transitions are optically thin and the $^{12}CO/^{13}CO$ flux ratio is equivalent to the $^{12}C/^{13}C$ ratio, which is not always the case; in the case that the radio transitions are optically thick, the real $^{12}C/^{13}C$ ratio is generally underestimated.

We will discuss the stars in the sample separately, according to their being M- or C-star. We do enter into the discussion of the possible origin of J stars, i.e. the carbon-rich objects in the sample with unusually low (below 15) $^{12}C/^{13}C$ ratios: these sources, as discussed in Section 6.3.2, likely belong to binary systems; thus, they cannot be understood on the basis of the single star models used here.

6.3.1 O-rich M-type AGB stars

The carbon ratio of these objects ($^{12}CO/^{13}CO \sim 6$–7) exhibits the signature of HBB, tracing the equilibria of proton-capture nucleosynthesis. As shown in Fig. 11 (see the left-hand panel), this is a common behaviour of all the models of initial mass above 3 $M_\odot$ discussed here.

The possibility that these objects descend from stars with mass just above the threshold required to activate HBB, i.e. 3.5 $M_\odot$, is

Table 3. Sample sources discussed in detail in Section 6.3 with their spectral type (S-type), the derived $^{12}C/^{13}C$ (assumed to be equal to the measured $^{12}CO/^{13}CO$) and computed absolute magnitude given by Ramstedt & Olofsson (2014). In the last column are shown the predicted numbers of end-of-mission *Gaia* observations. Stars with parallax measurements by *Hipparcos* or by more precise estimates as VLBI maser spot astrometry are labelled with an asterisk.

Name	S-type	$^{12}C/^{13}C$	$L/L_\odot$	N_G
IRC+10529	M	7	10 600	57
IRC+50137	M	6	9900	46
R Leo*	M	6	2500	30
GX Mon	M	11	8200	21
IK Tau	M	10	7700	48
IRC−30398	M	13	8900	21
IRC+10365	M	13	7700	39
CIT4	M	29	4000	57
IRC+60169	M	29	4000	82
IRC+70066	M	66	4000	76
SW Vir*	M	18	4000	45
RX Boo*	M	17	4000	47
W Hya*	M	10	6000	24
R Dor*	M	10	4000	36
RT Vir*	M	9	4500	39
R Cas*	M	19	4000	82
LP And	C	56	9600	68
V Cyg	C	38	6000	47
CW Leo	C	71	9800	27
RW Lmi	C	45	10 000	52
V384 Per	C	43	8300	43
UU Aur	C	100	4000	22

unlikely, because these stars reach the surface $^{12}C/^{13}C$ corresponding to the equilibrium of proton-capture nucleosynthesis only in the final TPs, thus for a limited fraction of the AGB life (see the track corresponding to the $3.5\,M_\odot$ case in the left-hand panel of Fig. 11).

We believe more probable that IRC+10529 and IRC+50137 descend from $M_{\rm init} \geq 4\,M_\odot$ stars and are currently evolving through the AGB phases following the ignition of HBB. This hypothesis is supported by the optical depth given by the authors, $\tau_{10} = 3$, indicating a large degree of obscuration, thus the presence of great amounts of silicate dust in the wind. The mass-loss rates indicated by Ramstedt & Olofsson (2014, in the range $10^{-5}\,M_\odot\,{\rm yr}^{-1} < \dot{M} < 3 \times 10^{-5}\,M_\odot\,{\rm yr}^{-1}$) rule out very massive progenitors, which shifts our attention towards $M_{\rm init} \sim 4\,M_\odot$ objects. This conclusion is further supported by statistical arguments, based on the duration of the AGB phase of stars of different masses, reported in Table 1 and in the bottom-right panel of Fig. 1.

If this interpretation proves correct, the luminosity expected is $L \sim 2 \times 10^4\,L_\odot$, significantly higher than those adopted by the authors ($L \sim 10^4\,L_\odot$, see Table 3).

R Leo exhibits a surface $^{12}C/^{13}C = 6$, similar to IRC+10529 and IRC+50137, indicating that the surface material was exposed to CN cycling. Unlike IRC+10529 and IRC+50137, the star is not heavily obscured ($\tau_{10} = 0.03$) and the given mass-loss rate ($10^{-7}\,M_\odot\,{\rm yr}^{-1}$) is a factor of ∼100 smaller.

The possibility that R Leo is currently experiencing HBB is not supported by the latter two pieces of evidence, unless it is currently evolving through a phase when mass-loss and dust production are temporarily interrupted. If this is the case, the luminosity should be not below $L \sim 2 \times 10^4\,L_\odot$, almost a factor of 10 higher than the value indicated by Ramstedt & Olofsson (2014).

An alternative possibility is that this star descends from an $M_{\rm init} \sim 1.5$–$2\,M_\odot$ progenitor and is currently evolving through the initial AGB phases, before becoming a carbon star. Cool bottom burning during red giant branch (RGB) ascending might account for the reduction of $^{12}C/^{13}C$: this process, proposed by Boothroyd & Sachmann (1999), is originated by deep circulation mixing below the base of the convective envelope, and has the effects of mixing material enriched in ^{13}C and depleted in ^{12}C to the surface. A problem with this interpretation is that the observed $^{12}C/^{13}C$ is smaller than the lowest predictions from cool bottom burning modelling, i.e. $^{12}C/^{13}C \sim 10$.

GX Mon, IK Tau, IRC−30398 and IRC+10365 share several properties in common with IRC+10529 and IRC+50137: the measured $^{12}C/^{13}C$ shows up the effects of HBB and the optical depths, in the range $0.5 < \tau_{10} < 1$, trace the presence of significant quantities of silicate dust in the circumstellar envelope. We discuss these four stars separately, because the carbon ratios given by the authors, $^{12}C/^{13}C \sim 10$, are higher than expected on the basis of a pure CNO equilibrium, although the errors associated with individual abundances are compatible with a pure HBB chemistry. In the latter case, the interpretation of these sources would be similar to what was proposed earlier in this section for IRC+10529 and IRC+50137.

Alternatively, the large degrees of obscuration and carbon isotopic ratios $^{12}C/^{13}C \sim 10$ are obtained in the final AGB phases of $M_{\rm init} \sim 4\,M_\odot$ stars (see the $4\,M_\odot$ track in the left-hand panel of Fig. 11): the interpretation of these stars would be similar to the scenario proposed for AFGL 5379 and OH 26.5+0.6, in Section 6.1. The effective temperatures of the stars in the late AGB phases, $T_{\rm eff} \sim 2200$ K, are only slightly in excess of the temperatures indicated by Ramstedt & Olofsson (2014).

According to this scenario, the stars in this group should have present masses of the order of ∼1–$1.5\,M_\odot$. The expected luminosity is $L \sim 2 \times 10^4\,L_\odot$, a factor of 2 higher than proposed by Ramstedt & Olofsson (2014).

CIT4, IRC+60169 and IRC+70666 have $^{12}C/^{13}C$ ratios in the range $20 < {}^{12}C/^{13}C < 60$. They exhibit a significant degree of obscuration, with $0.3 < \tau_{10} < 1$, revealing the presence of silicate dust in the wind. While the large $^{12}C/^{13}C$'s indicate the effects of TDU, the presence of significant quantities of dust in the circumstellar envelope suggests advanced AGB stages of stars with progenitors of mass above $\sim 3.5\,M_\odot$: indeed lower mass stars reach the C-star stage, and little dust formation occurs in the early AGB phases, when the star is still oxygen-rich.

The carbon ratios and the mass-loss rates proposed by Ramstedt & Olofsson (2014) are reproduced by models with initial mass $M_{\rm init} \sim 3.5\,M_\odot$, just above the threshold to activate HBB; as shown in Fig. 11 (see the left-hand panel), these stars first experience a series of TDU events, favouring the increase in the surface ^{12}C, then produce ^{13}C via HBB. If this understanding is correct, the stars should have a current mass of $\sim 2.5\,M_\odot$ and a luminosity of $L \sim 1.5 \times 10^4\,L_\odot$.

Alternatively, the degree of obscuration and the rate of mass-loss proposed are reproduced by models of initial mass 4–$4.5\,M_\odot$, in the final evolutionary phases: similarly to the stars discussed in the previous point, the large $^{12}C/^{13}C$ might be the effect of late TDU episodes, occurring when HBB is turned off. If this interpretation is correct, we may fix the current mass and luminosity of these stars, that are, respectively, $M \sim 1.5\,M_\odot$ and $L \sim 2 \times 10^4\,L_\odot$.

In both cases, the luminosities expected are significantly in excess of the suggestion by the authors, which give $L = 4000\,L_\odot$ for IRC+60169 and IRC+70666.

SW Vir and RX Boo have $^{12}C/^{13}C \sim 20$, which is compatible with the chemistry of any star at the beginning of the AGB phase, when the chemical composition was modified solely by the first and, possibly, the second dredge-up episodes.

Based on the luminosities given by the authors, $L = 4000\,L_{\odot}$, we conclude that SW Vir and RX Boo descend from 1.5–2.0 $M_{\odot}$ objects and are currently at the beginning of the AGB evolution, before reaching the C-star stage. This interpretation is also in agreement with the very small optical depths given by Ramstedt & Olofsson (2014), $\tau_{10} \sim 0.02$–0.03.

However, the same isotopic ratios and small degree of obscuration are also reproduced by higher mass models in the early AGB phases, before the ignition of HBB. In this case, the luminosities would be $L \sim 10^4\,L_{\odot}$, larger than the values given by Ramstedt & Olofsson (2014).

Concerning W Hya, R Dor, RT Vir and R Cas, the material in the surface regions of these stars was exposed to partial CN cycling, as confirmed by the observed isotopic carbon ratios, $^{12}C/^{13}C \sim 10$. The luminosities given by the authors for these stars are in the range $4 \times 10^3\,L_{\odot} < L < 6 \times 10^3\,L_{\odot}$. If these luminosities will be confirmed by precise distance measurements (see the next section), the possibility that the observed $^{12}C/^{13}C$'s are determined by HBB would be ruled out because significantly smaller than those reached by the stars experiencing HBB. A valid alternative is that the stars in this group descend from low-mass progenitors: the main arguments supporting this conclusion are (a) all the stars of mass in the range $1\,M_{\odot} < M_{\rm init} < 3\,M_{\odot}$ evolve at luminosities similar to those observed, in the AGB phases previous to the increase in the surface ^{12}C via TDU (the latter mechanism would increase the $^{12}C/^{13}C$, far above the observed values); (b) the degree of obscuration and the mass-loss rate indicated by Ramstedt & Olofsson (2014) are very small, which is typical of the AGB evolution of low-mass stars, before the C-rich phase is reached.

On the theoretical side, we expect that the surface $^{12}C/^{13}C$ of these objects is modified by the first dredge-up, after which according to standard modelling of mixing we have $^{12}C/^{13}C \sim 20$; this is a factor of $\sim$2 higher than observed. A solution for this discrepancy could be that the stars in this group experienced cool bottom processing during the RGB ascending (Boothroyd & Sachmann 1999).

6.3.2 *C-rich N-type AGB stars*

LP And, V Cyg, CW Leo, RW LMi, V384 Per and UU Aur have a surface C/O above unity, the signature of repeated TDU events. The mass-loss rate is correlated to the surface $^{12}C/^{13}C$, which spans the range $40 < {}^{12}C/^{13}C < 100$; this is what we expect from the AGB evolution of low-mass stars, as discussed in Section 3.2. These six objects are therefore experiencing advanced evolutionary phases of the AGB life, after becoming carbon stars.

The observed $^{12}C/^{13}C$'s are attained by all the stars with initial mass in the range $1.5\,M_{\odot} \leq M_{\rm init} \leq 3\,M_{\odot}$, although the luminosities and the mass-loss rates given by Ramstedt & Olofsson (2014) suggest 1.5–2 $M_{\odot}$ progenitors. The optical depths given by the authors are in the range $0.2 < \tau_{10} < 1$, which indicates the presence of significant quantities of carbon dust in the wind; this is expected on the basis of AGB+dust modelling of stars evolving through the C-star phase (Dell'Agli et al. 2014).

The interpretation of UU Aur and V Cyg poses some problems. UU Aur has the largest $^{12}C/^{13}C$ in the overall sample, namely $^{12}C/^{13}C = 100$. Such large carbon abundances are reached by all the low-mass star models considered here. The luminosity of this object is an issue though: while according to our modelling the C-star stage is not reached as far as the luminosity is below $\sim$8000 $L_{\odot}$, Ramstedt & Olofsson (2014) indicate $L = 4000\,L_{\odot}$.

The luminosity of V Cyg given by Ramstedt & Olofsson (2014), $L = 6000\,L_{\odot}$, is also not reproduced by our models. If confirmed, the low luminosities of these two objects would be a strong indication that TDU is more efficient in the AGB stars of solar metallicity, compared to the predictions given here.

6.3.3 *S-type AGB stars*

The sample by Ramstedt & Olofsson (2014) includes 17 S-type stars, with a surface C/O around unity. The interpretation of these objects is not straightforward, because the $^{12}C/^{13}C$ and the luminosities given in the above paper are not consistent with our predictions. Concerning the chemical composition, fig. 2 in Ramstedt & Olofsson (2014) shows that the average $^{12}C/^{13}C$ of this group of stars is slightly above 20, whereas according to our models carbon stars should have $^{12}C/^{13}C > 50$. This is shown in Fig. 7 (right-hand panel); note that the same chemistry is also expected on the basis of C15 models, which adds more robustness to this general conclusion. This systematic difference can be explained only by invoking some ad hoc mechanism, such as cool bottom burning, acting to increase the ^{13}C in the envelope of low-mass stars before they become enriched in ^{12}C; we believed this possibility unlikely though, because all the S-stars in the Ramstedt & Olofsson (2014) sample present such a low $^{12}C/^{13}C$, thus indicating that this mechanism should be active in all low-mass stars. Alternatively, the circumstellar $^{12}C/^{13}C$ is not a reliable tracer of the surface C/O ratio, at least for S-type stars. The interpretation of the results by Ramstedt & Olofsson (2014) is further complicated by the differences among the luminosities expected based on our models and those given by the authors. As discussed in Section 3.2, and shown in Fig. 7, carbon stars of solar chemistry are expected to evolve at luminosities $L > 8000\,L_{\odot}$. This is at odds with the luminosities adopted by Ramstedt & Olofsson (2014, see their table 1), which are in the range 4000–12 000 $L_{\odot}$. Note that the use of C15 models (shown in the same figure) would hardly improve this mismatch, as in that case luminosities not below 7000 $L_{\odot}$ are expected.

6.4 Distance estimates within *Gaia* mission

This detailed analysis shows that reliable measurements of the distance of Galactic AGB, especially of those with recent estimates of CNO elemental and isotopic abundances, are urgently needed. The knowledge of the distance will allow a robust determination of the luminosity, which, as discussed in the previous sections, is crucial to the characterization of the observed stars in terms of mass and evolution.

In Table 3, we summarized the characteristics of the Ramstedt & Olofsson (2014) sample discussed in details in Section 6.3. The authors report the predicted absolute luminosity; however, only in a few cases (starred with an asterisk in the table) the luminosities were estimated from accurate *Hipparcos* parallax measurements or by very long baseline interferometry (VLBI) maser spot astrometry. In all other cases, the luminosity was either derived from Groenewegen & Whitelock (1996) period–luminosity relation (Mira variables) or assumed to be equal to 4000 $L_{\odot}$ (semi-regular, irregular variables, variables of unknown type or period). The uncertainty in the observed luminosity estimates makes the comparison between observed and predicted luminosities inconclusive.

As mentioned in the introduction, this problem will be addressed when *Gaia* astrometry for these stars will be available.[6] The accuracy of *Gaia* parallaxes depends in a complicated way on several factors: number of observations, environment (i.e. stellar density), brightness, colour and so on. The number of end-of-mission observations based on *Gaia* scanning law[7] is reported in the last column of Table 3. A good fraction of the Ramstedt & Olofsson (2014) sample stars will probably be observed enough times to reach the nominal astrometric error for bright stars of their spectral type ($\sim\sigma_\pi = 10\,\mu$as). However, given that most of the stars in our sample are Mira or semi-regular variables, it is not possible at present to evaluate the actual parallax accuracy for them. If accurate parallaxes will be available, then it will be possible to derive accurate luminosities, to discriminate among different model scenarios and to assign an evolutionary mass in several cases.

7 CONCLUSIONS

We present solar metallicity models of the AGB phase of stars with mass in the range $1\,M_\odot < M < 8\,M_\odot$. This investigation integrates previous explorations by our group, focused on sub-solar chemistries.

The main physical and chemical properties of AGB stars are extremely sensitive to the stellar mass. A threshold mass $M \sim 3$–$3.5\,M_\odot$ separates two distinct behaviours.

The chemical composition of stars of mass $M \leq 3\,M_\odot$ is altered by the TDU mechanism, which favours a gradual increase in the surface carbon content. We find that the stars with mass in the range $1.5\,M_\odot \leq M \leq 3\,M_\odot$ become carbon stars during the AGB phase. Once the C-star stage is reached, the consumption of the envelope is accelerated by the expansion of the external regions and by the effects of radiation pressure acting on the carbonaceous dust particles in the circumstellar envelope. These effects prevent further significant enrichment in the surface carbon, keeping the C/O ratio below ∼1.5. The gas ejected by these stars is enriched in carbon and nitrogen by a factor of ∼3 compared to the material from which the stars formed. The luminosities of carbon stars fall in the range $8 \times 10^3\,L_\odot < L < 1.2 \times 10^4\,L_\odot$.

Stars of mass $M > 3\,M_\odot$ experience HBB at the bottom of the convective envelope. The strength of the HBB increases with the mass of the star. The pollution from these stars reflects the equilibrium abundances of the HBB nucleosynthesis experienced. On general grounds, we expect carbon-poor and nitrogen-rich ejecta, owing to CN cycling. In stars of mass above $\sim 5\,M_\odot$, the HBB temperatures are sufficiently large to activate the full CNO and the Ne–Na nucleosynthesis: the gas expelled by these stars is enriched in sodium, whereas the oxygen content is smaller than it was when the star formed. These stars are expected to evolve as lithium-rich sources for a significant fraction of the AGB phase.

The comparison with results in the literature outlines some similarities but also significant differences, particularly for what regards the strength of the HBB experienced, thus the luminosities at which these stars evolve and the kind of pollution expected. The carbon, nitrogen and sodium content of stars of mass above $3\,M_\odot$ are extremely different from the results from other research teams, stressing the importance of confirmation from the observations.

We compare the models presented here with the CNO elemental and isotopic abundances in different types of Galactic AGB stars as estimated from observational data at very different wavelengths (from the optical to the radio domain); this part of the research has the double scope of adding more robustness to the present results and to characterize to stars observed, in terms of mass and age of the progenitors. The comparison with the observations is hampered by the unknown distances of the sources discussed.

[6] Seven stars of the Ramstedt & Olofsson (2014) sample will probably already be included in *Gaia*'s first data release, foreseen by the end of summer 2016, which will include parallaxes for the large majority of the *Hipparcos* and Tycho-2 stars.

[7] Computed with the Observation Forecast Tool available at http://gaia.esac.esa.int/gost/index.jsp

ACKNOWLEDGEMENTS

MDC acknowledges the contribution of the FP7 SPACE project ASTRODEEP (Ref. No. 312725), supported by the European Commission. DAGH was funded by the Ramón y Cajal fellowship number RYC-2013-14182 and he acknowledges support provided by the Spanish Ministry of Economy and Competitiveness (MINECO) under grant AYA-2014-58082-P. FD acknowledges support from the Observatory of Rome.

REFERENCES

Arnould M., Goriely S., Jorissen A., 1999, A&A, 347, 572
Becker S. A., Iben I., Jr, 1980, ApJ, 237, 111
Blöcker T., 1995, A&A, 297, 727
Blöcker T., Schöenberner D., 1991, A&A, 244, L43
Boothroyd A. I., Sachmann I.-J., 1999, ApJ, 510, 232
Cameron A. G. W., Fowler W. A., 1971, ApJ, 164, 111
Canuto V. M. C., Mazzitelli I., 1991, ApJ, 370, 295
Cloutmann L., Eoll J. G., 1976, ApJ, 206, 548
Cristallo S., Straniero O., Gallino R., Piersanti L., Dominguez I., Lederer M. T., 2009, ApJ, 696, 797
Cristallo S., Straniero O., Piersanti L., Gobrecht D., 2015, ApJS, 219, 40
Dell'Agli F., Ventura P., García-Hernández D. A., Schneider R., Di Criscienzo M., Brocato E., D'Antona F., Rossi C., 2014, MNRAS, 442, L38
Dell'Agli F., Ventura P., Schneider R., Di Criscienzo M., García-Hernández D. A., Rossi C., Brocato E., 2015a, MNRAS, 447, 2992
Dell'Agli F., García-Hernández D. A., Ventura P., Schneider R., Di Criscienzo M., Rossi C., 2015b, MNRAS, 454, 4235
Dell'Agli F., Di Criscienzo M., Boyer M. L., García-Hernández D. A., 2016, MNRAS, 460, 4230
Doherty C. L., Gil-Pons P., Lau H. H. B., Lattanzio J. C., Siess L., 2014, MNRAS, 437, 195
Gail H.-P., Sedlmayr E., 1999, A&A, 347, 594
Garcia-Berro E., Iben I. J., 1994, ApJ, 434, 306
Garcia-Berro E., Ritossa C., Iben I. J., 1997, ApJ, 485, 765
García-Hernández D. A., García-Lario P., Plez B., Manchado A., D'Antona F., Lub J., Habing H., 2007, A&A, 462, 711
García-Hernández D. A. et al., 2009, ApJ, 705, L31
Grevesse N., Sauval A. J., 1998, Space Sci. Rev., 85, 161
Groenewegen M. A. T., de Jong T., 1993, A&A, 267, 410
Groenewegen M. A. T., Whitelock P. A., 1996, MNRAS, 281, 1347
Herwig F., 2005, ARA&A, 43, 435
Iben I., Jr, 1982, ApJ, 260, 821
Iben I., Jr, Renzini A., 1983, ARA&A 21, 271
Iglesias C. A., Rogers F. J., 1996, ApJ, 464, 943
Izzard R. G., Tout C. A., Karakas A. I., Pols O. R., 2004, MNRAS, 350, 407
Jordi C. et al., 2010, A&A, 523, A48
Justtanont K., Teyssier D., Barlow M. J., Matsuura M., Swinyard B., Waters L. B. F. M., Yates J., 2013, A&A, 556, A101
Justtanont K. et al., 2012, A&A, 537, A144
Karakas A. I., Lattanzio J. C., 2014, PASA, 31, e030

Karakas A. I., Lugaro M., 2016, ApJ, 825, 26
Karakas A. I., Lattanzio J. C., Pols O. R., 2002, PASA, 19, 515
Kobayashi C., Karakas A. I., Umeda H., 2011, MNRAS, 414, 3231
Lattanzio J. C., 1986, ApJ, 311, 708
Marigo P., 2002, A&A, 387, 507
Marigo P., Aringer B., 2009, A&A, 508, 1538
Marigo P., Girardi L., 2007, A&A, 469, 23
Marigo P., Girardi L., Bressan A., 1999, A&A, 344, 123
Marigo P., Bressan A., Girardi L., Aringer B., Gullieuszik M., Groenewegen M. A. T., 2011, in Kerschbaum F., Lebzelter T., Wing R. F., eds, ASP Conf. Ser. Vol. 445, Why Galaxies Care about AGB Stars II: Shining Examples and Common Inhabitants. Astron. Soc. Pac., San Francisco, p. 431
Mowlavi N., 1999, A&A, 350, 73
Ramstedt S., Olofsson H., 2014, A&A, 566, A145
Romano D., Karakas A. I., Tosi M., Matteucci F., 2010, A&A, 522, A32
Rosenfield P. et al., 2014, ApJ, 790, 22
Rosenfield P., Marigo P., Girardi L., Dalcanton J. J., Bressan A., Williams B. F., Dolphin A., 2016, ApJ, 822, 73
Sackmann I. J., Boothroyd A. I., 1992, ApJ, 392, L71
Santini P. et al., 2014, A&A, 562, A30
Schwarzschild M., Harm R., 1965, ApJ, 142, 855
Schwarzschild M., Harm R., 1967, ApJ, 145, 496
Siess L., 2006, A&A, 448, 717
Siess L., 2007, A&A, 476, 893
Siess L., 2009, A&A, 497, 463
Siess L., 2010, A&A, 512, A10
Siess L., Arnould M., 2008, A&A, 489, 395
Stancliffe R. J., Izzard R. G., Tout C. A., 2005, MNRAS, 356, L1
Valiante R., Schneider R., Bianchi S., Andersen A., Anja C., 2009, MNRAS, 397, 1661
Valiante R., Schneider R., Salvadori S., Bianchi S., 2011, MNRAS, 416, 1916
Ventura P. D'Antona F., 2011, MNRAS, 410, 2760
Ventura P., D'Antona F., 2005a, A&A, 431, 279
Ventura P., D'Antona F., 2005b, A&A, 439, 1075
Ventura P., D'Antona F., 2006, A&A, 457, 995
Ventura P., D'Antona F., 2008, MNRAS, 385, 2034
Ventura P., D'Antona F., 2009, MNRAS, 499, 835
Ventura P., Marigo P., 2009, MNRAS, 399, L54
Ventura P., Marigo P., 2010, MNRAS, 408, 2476
Ventura P., Zeppieri A., Mazzitelli I., D'Antona F., 1998, A&A, 334, 953
Ventura P., D'Antona F., Mazzitelli I., 2000, A&A, 363, 605
Ventura P., D'Antona F., Mazzitelli I., Gratton R., 2001, ApJ, 550, L65
Ventura P., Di Criscienzo M., Carini R., D'Antona F., 2013, MNRAS, 431, 3642
Ventura P., Di Criscienzo M. D., D'Antona F., Vesperini E., Tailo M., Dell'Agli F., D'Ercole A., 2014a, MNRAS, 437, 3274
Ventura P., Dell'Agli F., Di Criscienzo M., Schneider R., Rossi C., La Franca F., Gallerani S., Valiante R., 2014b, MNRAS, 439, 977
Ventura P., Karakas A. I., Dell'Agli F., Boyer M. L., García-Hernández D. A., Di Criscienzo M., Schneider R., 2015, MNRAS, 450, 3181
Ventura P., Karakas A. I., Dell'Agli F., García-Hernández D. A., Boyer M. L., Di Criscienzo M., 2016, MNRAS, 457, 1456
Vlemmings W. H. T. et al., 2013, A&A, 556, L1
Wachter A., Schröder K. P., Winters J. M., Arndt T. U., Sedlmayr E., 2002, A&A, 384, 452
Wachter A., Winters J. M., Schröder K. P., Sedlmayr E., 2008, A&A, 486, 497

This paper has been typeset from a TEX/LATEX file prepared by the author.